

Mock data sets for the Eboss and DESI Lyman- α forest surveys

Thomas Etourneau,^a Jean-Marc Le Goff,^{a,1} James Rich,^{a,2}
Ting Tan,^b Andrei Cuceu,^{c,3} S. Ahlen,^d E. Armengaud,^a
D. Brooks,^e T. Claybaugh,^f A. de la Macorra,^g P. Doel,^e
A. Font-Ribera,^h J. E. Forero-Romero,^{i,j} S. Gontcho A
Gontcho,^f A. X. Gonzalez-Morales,^{k,l} H. K. Herrera-Alcantar,^l
K. Honscheid,^{c,m} T. Kisner,^f M. Landriau,^f M. Manera,^{h,n}
P. Martini,^{c,o} R. Miquel,^{h,p} A. Muñoz-Gutiérrez,^g J. Nie^q
I. Pérez-Ràfols,^r C. Poppett,^{f,s} C. Ravoux,^{a,t} M. Rezaie^u
G. Rossi,^v E. Sanchez,^w M. Schubnell,^x J. Stermer,^b G. Tarlé^x
M. Walther,^{y,z} Z. Zhou^q

^aIRFU, CEA, Université Paris-Saclay, F-91191 Gif-sur-Yvette, France

^bSorbonne Université, CNRS/IN2P3, Laboratoire de Physique Nucléaire et de Hautes Energies (LPNHE), FR-75005 Paris, France

^cCenter for Cosmology and AstroParticle Physics, The Ohio State University, 191 West Woodruff Avenue, Columbus, OH 43210, USA

^dPhysics Dept., Boston University, 590 Commonwealth Avenue, Boston, MA 02215, USA

^eDepartment of Physics & Astronomy, University College London, Gower Street, London, WC1E 6BT, UK

^fLawrence Berkeley National Laboratory, 1 Cyclotron Road, Berkeley, CA 94720, USA

^gInstituto de Física, Universidad Nacional Autónoma de México, Cd. de México C.P. 04510, México

^hInstitut de Física d'Altes Energies (IFAE), The Barcelona Institute of Science and Technology, Campus UAB, 08193 Bellaterra Barcelona, Spain

ⁱDepartamento de Física, Universidad de los Andes, Cra. 1 No. 18A-10, Edificio Ip, CP 111711, Bogotá, Colombia

^jObservatorio Astronómico, Universidad de los Andes, Cra. 1 No. 18A-10, Edificio H, CP 111711 Bogotá, Colombia

^kConsejo Nacional de Ciencia y Tecnología, Av. Insurgentes Sur 1582. Colonia Crédito Constructor, Del. Benito Juárez C.P. 03940, México D.F. México

^lDepartamento de Física, Universidad de Guanajuato - DCI, C.P. 37150, Leon, Guanajuato, México

¹Corresponding author.

²Corresponding author.

³NASA Einstein Fellow.

^mDepartment of Physics, The Ohio State University, 191 West Woodruff Avenue, Columbus, OH 43210, USA

ⁿDepartament de Física, Serra Hünter, Universitat Autònoma de Barcelona, 08193 Bellaterra (Barcelona), Spain

^oInstitució Catalana de Recerca i Estudis Avançats, Passeig de Lluís Companys, 23, 08010 Barcelona, Spain

^pInstitució Catalana de Recerca i Estudis Avançats, Passeig de Lluís Companys, 23, 08010 Barcelona, Spain

^qNational Astronomical Observatories, Chinese Academy of Sciences, A20 Datun Rd., Chaoyang District, Beijing, 100012, P.R. China

^rDepartament de Física, EEBE, Universitat Politècnica de Catalunya, c/Eduard Maristany 10, 08930 Barcelona, Spain

^sSpace Sciences Laboratory, University of California, Berkeley, 7 Gauss Way, Berkeley, CA 94720, USA

^tAix Marseille Univ, CNRS/IN2P3, CPPM, Marseille, France

^uDepartment of Physics, Kansas State University, 116 Cardwell Hall, Manhattan, KS 66506, USA

^vDepartment of Physics and Astronomy, Sejong University, Seoul, 143-747, Korea

^wCIEMAT, Avenida Complutense 40, E-28040 Madrid, Spain

^xDepartment of Physics, University of Michigan, Ann Arbor, MI 48109, USA

^yExcellence Cluster ORIGINS, Boltzmannstrasse 2, D-85748 Garching, Germany

^zUniversity Observatory, Faculty of Physics, Ludwig-Maximilians-Universität, Scheinerstr. 1, 81677 München, Germany

E-mail: jmlegoff@cea.fr, james.rich@cea.fr

Abstract. We present a publicly-available code to generate sets of mock Lyman- α ($\text{Ly}\alpha$) forest data that have realistic large-scale correlations including those due to the Baryonic Acoustic Oscillations (BAO). The primary purpose of these mocks is to test the analysis procedures of the Extended Baryon Oscillation Survey (eBOSS) and the Dark Energy Spectroscopy Instrument (DESI) surveys. The transmitted flux fraction, $F(\lambda)$, of background quasars due to $\text{Ly}\alpha$ absorption in the intergalactic medium (IGM) is simulated using the Fluctuating Gunn-Petterson Approximation (FGPA) applied to Gaussian random fields produced through the use of fast Fourier transforms (FFT). The output includes the IGM- $\text{Ly}\alpha$ transmitted flux fraction along quasar lines of sight and a catalog of high-column-density systems appropriately placed at high-density regions of the IGM. This output serves as input to additional code that superimposes the IGM transmission on realistic quasar spectra, adds absorption by high-column-density systems and metals, and simulates instrumental transmission and noise. Redshift space distortions (RSD) of the flux correlations are implemented by including the large-scale velocity-gradient field in the FGPA resulting in a correlation function of $F(\lambda)$ that can be accurately predicted. One hundred realizations have been produced over the 14,000 deg^2 DESI survey footprint with 100 quasars per deg^2 . The analysis of these realizations shows that the correlations of $F(\lambda)$ follows the prediction within the accuracy of eBOSS survey. The most time-consuming part of the mock production occurs before application of the FGPA, and the existing pre-FGPA forests can be used to easily produce new mock sets with modified redshift-dependent bias parameters or observational conditions.

Contents

1	Introduction	1
2	Mock generation	4
2.1	Matter-density, velocity and velocity-gradient boxes	4
2.2	Quasar generation	5
2.3	Gaussian fields along lines of sight	5
2.4	FGPA	7
2.5	The expected auto-correlation function of the mocks	8
2.6	Adjusting mock parameters	9
2.7	High column density systems (HCD)	11
2.8	Metals	12
3	Implementation and production	12
4	Analysis of the mock data sets	13
4.1	Analysis procedure of forest correlations	14
4.2	Forest correlations in the raw mocks	15
4.3	Forest correlations in the cooked mocks	18
4.4	QSO auto-correlations	25
5	Conclusions	26
A	The z-dependence of quasar correlation function	27
B	Small scale fluctuations	28

1 Introduction

The Lyman- α ($\text{Ly}\alpha$) forest is a series of absorption features visible in quasar spectra due to the presence of neutral hydrogen (HI) in the intergalactic medium (IGM). The Baryon Oscillation Spectroscopy Survey (BOSS) [1] and the extended Baryon Oscillation Spectroscopy Survey (eBOSS) [2] obtained the spectra of over $\approx 200,000$ forests. This permitted the study of cosmological large-scale structure (LSS) through correlations of absorption between different forests [3–8] and through correlations between forests and quasars [9–12]. These so-called 3d correlations have been used to study baryonic acoustic oscillations (BAO) with the most recent results found by a combination of BOSS and eBOSS data [13] yielding constraints on the parameters of cosmological models [14]. The 3d correlations have also been used to study the clustering of Damped $\text{Ly}\alpha$ systems (DLAs) [15, 16] and of the circumgalactic medium [17]. Finally, correlations within individual forests allow the measurement of the so-called 1d power spectrum, yielding constraints on the amplitude and shape of the power spectrum at high redshift [18–22]. All of these studies are being continued with the currently running Dark Energy Spectroscopy Instrument [23] which is expected to make considerable improvements in precision of cosmological parameters [24].

Most studies of large-scale structure have used galaxies as discrete tracers of the cosmological density field. In contrast to galaxies, $\text{Ly}\alpha$ absorption is a continuous probe of the density and a single quasar spectra provides a proxy for matter density along the quasar line-of-sight. On the other hand due to the relation between the transmitted flux fraction and the $\text{Ly}\alpha$ optical depth, $F = \exp(-\tau)$, the bias is negative and its absolute value is much smaller than unity.

Mock data sets are needed to test the analysis procedures that lead to the Ly α forest correlations. These mock data sets must cover hundreds of $h^{-3}\text{Gpc}^3$, while the absorption in a quasar spectrum probes the intergalactic medium at the Jean's scale, i.e. around $100h^{-1}\text{ kpc}$. It is not possible to perform hydrodynamical or N-body simulations with such volumes and resolutions. We are therefore limited to generating Gaussian random fields with a correlation close to that of the data. The state-of-the-art mock sets presented here are not yet sufficiently realistic to be explicitly used in the analysis of real data by, for instance, providing a usable covariance matrix as is done in galaxy data sets. Rather, they are used to demonstrate that the analysis procedure leads to estimates of physical parameters that are near those of the model used to generate the mocks and that the reported uncertainties are consistent with the variations observed between independent mock sets. Most importantly, we want to demonstrate that the BAO peak position is correctly determined on average with a precision at the 1% level. The other physical parameters related to the broadband shape of the correlation functions are of less importance and we will see that the mocks confirm the accuracy of their determination only at the 10% level. The mocks are also used to study astrophysical effects, such as those due to the presence of high column density (HCD) systems or metal lines in the Ly α forest.

The BOSS survey used two sets of mocks, the first of which [25, 26] used a Cholesky decomposition of the correlation matrix between pairs for forest pixels and generated a 3d correlated field only along the quasar lines-of-sight. This approach allows for the generation of mock data sets with whatever desired correlation function, e.g. including the significant non-linear effects on small scales. However, it results in no cross-correlation between the flux transmission in the Ly α pixels and the quasar positions, so these mocks were not useful for studies of the forest-quasar cross-correlation.

In order to include quasar-forest correlations, the second set of BOSS mocks [11] was produced for the final BOSS analysis. They were based on a simpler approach, originally developed to study BOSS Ly α analysis feasibility [27]. The Gaussian-random-field defining density fluctuations was generated on a 3-dimensional grid with spacing $3.2\ h^{-1}\text{Mpc}$, defining a parallelepipedic box with cubic "voxels" of volume $(3.2\ h^{-1}\text{Mpc})^3$. Redshift space distortion (RSD) were implemented using the corresponding velocity grid. Real forest pairs have fixed angular separation so the transverse separation of pairs depends on wavelength. In these mocks, the approximation of parallel lines-of-sight was made, so the separation is wavelength independent. The positions of the quasars were originally [27] drawn randomly over the box, so for cross-correlation studies [11] the code was modified such that the quasar positions are selected in voxels with a density above a given threshold.

The eBOSS auto-correlation [28] analysis using SDSS data release 14 (DR14) made use of BOSS Cholesky mocks [25] while the cross-correlation [29] analysis used the second set of BOSS mocks with cross-correlation but the approximation of parallel lines-of-sight [11].

Two mock projects were developed for the final eBOSS analysis using SDSS data release 16 (DR16) and for DESI. They use basically the same approach as the second set of BOSS mocks with the main improvement that the lines-of-sight are no longer parallel. The first project, described in [30] produced what are referred to informally as "London mocks" or "Ly α Colore mocks". This project used the same approach as the second set of BOSS mocks to select quasar locations and implement the RSD. They were used to validate the analysis of the final eBOSS BAO study [13]. The second project presented here produced what are referred to informally as "Saclay mocks". In this project we have implemented RSD by including the large-scale velocity gradient fluctuations in the FGPA, allowing for a prediction of the mock correlation function. We use a lognormal field to select quasar locations in a way that significantly improves the quasar auto-correlation at small separation. These mocks have been used in the determination of the

Table 1. Cosmological parameters [34] of the flat Λ CDM model used in the Mock generation.

Parameter	value	
Ω_M	0.3147	density of non-relativistic matter
$\Omega_c h^2$	0.1198	density of cold dark matter
$\Omega_b h^2$	0.02233	density of baryons
h	0.6737	Expansion rate $H_0/(100 \text{ km}^{-1} \text{ s}^{-1} \text{ Mpc}^{-1})$
$A_s \times 10^{10}$	3.043	Amplitude of scalar perterbations
n_s	0.9652	spectral index of scalar perturbations

eBOSS DLA detection efficiency [31] and to study the correlation of voids and the Ly α forest [32].

The production of realistic mocks is a four-step process. The first step is the calculation of IGM-Ly α transmission field along lines of sight to quasars. The second step is to add additional absorption due to HCDs and to metals. The third is to apply this transmission on realistic quasar spectra. Finally, the fourth step introduces instrumental noise and atmospheric transmission. This paper is primarily concerned with the IGM transmission of the first step. The remaining steps are briefly described here but more completely in [33].

Section 2 explains how the mock data sets are produced, using a Gaussian random field to generate the IGM absorption field and quasar positions. The procedures for generating HCDs and absorption by metals are also briefly discussed. Section 3 describes the implementation and the production of these mocks. Section 4 presents the results of the analysis of the mock sets that contain no HCDs or metals. The analysis of mock sets that include absorption by HCDs will be described in a forthcoming publication [Tan et al, in preparation]. Conclusions are drawn in Sect. 5. Several appendices describe some technical issues that were not detailed in section 2.

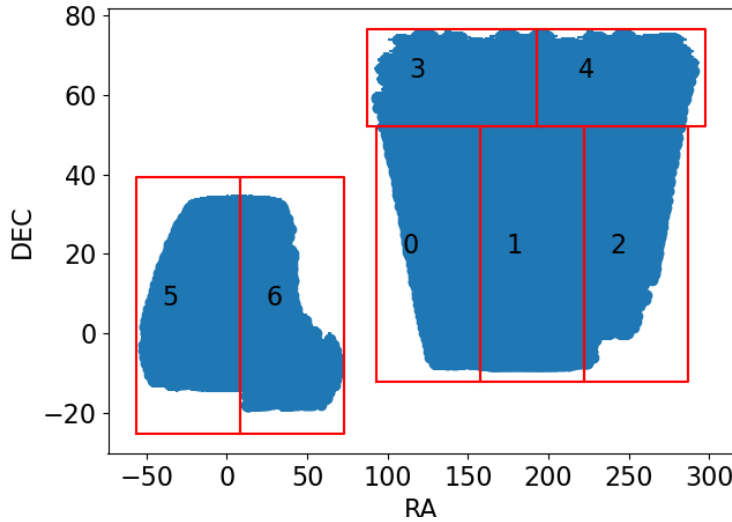


Figure 1. The position in (ra,dec) of the seven "chunks" containing the density, velocity, and velocity gradient boxes used to generate the mocks. The blue region is the DESI footprint (which includes the eBOSS footprint). Each box contains $2560 \times 2560 \times 1536$ cubic voxels of volume $(2.19h^{-1}\text{Mpc})^3$. The radial dimension has 1536 grid steps and covers the redshift range $1.5 < z < 3.8$. The boxes are adjacent at $z = 3.8$ and therefore overlap for $z < 3.8$.

2 Mock generation

We generate density and velocity fields in the DESI footprint by combining "boxes" of volume $V \approx 105(\text{Gpc}/h)^3$ containing $2560 \times 2560 \times 1536$ cubic voxels of $2.19 h^{-1}$ Mpc sides. The positioning of the boxes is shown in Fig. 1.

For each box, an independent normal Gaussian random variable, $\delta(\mathbf{r})$, is generated in each voxel of the box, which results in a constant power spectrum of the box, $P(k) = V_{\text{vox}}$, the volume of a voxel. We perform a 3d Fourier transform using a fast Fourier transform algorithm (FFT) [35], which results in a box in k -space with $\hat{\delta}(-\mathbf{k}) = [\hat{\delta}(\mathbf{k})]^*$, where we place hats on fields in k -space¹. For a power spectrum $P_0(\mathbf{k})$, multiplying each mode $\hat{\delta}(\mathbf{k})$ by $\sqrt{P_0(\mathbf{k})/V_{\text{vox}}}$ and applying inverse FFT results in a field in real space with power spectrum P_0 . For a given set of $\hat{\delta}(\mathbf{k})$ we thereby generate four physical fields with differing but related power spectra: the matter density field at $z = 0$ (Eq. 2.1) and three lognormal quasar-density fields at different redshifts (section 2.2). We also define, in k -space, boxes filled with the corresponding fields for the velocity (Eq. 2.2) and velocity gradient (Eq. 2.3) and apply inverse FFT to obtain the corresponding fields in real space. The details of these fields are given the following subsections.

2.1 Matter-density, velocity and velocity-gradient boxes

For each mode \mathbf{k} we introduce

$$\hat{\delta}_m(\mathbf{k}) = \sqrt{\frac{P_m(\mathbf{k})}{V}} \hat{\delta}(\mathbf{k}) , \quad (2.1)$$

where P_m is the matter power spectrum at $z = 0$ obtained using CAMB [36] with flat- Λ CDM parameters shown in Table 1. This results in a correlated Gaussian random field, δ_m , in real space with power spectrum P_m .

Within linear approximation, the velocity field in \mathbf{k} -space reads

$$\hat{v}_j(\mathbf{k}) = i f a H(z) \frac{k_j}{k^2} \hat{\delta}_m(\mathbf{k}) , \quad (2.2)$$

where $a = 1/(1+z)$, $f = d \ln G / d \ln a$ is the linear growth rate of structure with G the growth factor, and $H(z)$ is the Hubble parameter. We produce three boxes that contain the three coordinates, v_j , of the velocity field in real space at $z = 0$. After multiplying by a factor $f a H / (f a H)_{z=0}$ to go from $z = 0$ to the considered quasar redshift, these boxes provide the radial peculiar velocity, $v_{\parallel} = u_j v^j$, for a quasar line-of-sight with unit vector u_j . This velocity modifies the cosmological redshift and generates the associated redshift-space distortions (RSD) of the quasar auto-correlation function.

Still within linear approximation the velocity-gradient fluctuation in \mathbf{k} -space reads

$$\hat{\eta}_{pq}(\mathbf{k}) = f \frac{k_p k_q}{k^2} \hat{\delta}_m(\mathbf{k}) , \quad (2.3)$$

By applying inverse Fourier transform we produce 6 boxes that contains the resulting velocity gradient components in real space. The line-of-sight velocity gradient is then $\eta_{\parallel} = u_p u_q \eta^{pq}$.

¹We could have directly generated the $\hat{\delta}(\mathbf{k})$ box in k -space saving one FFT. We chose to use the more straightforward procedure of generating first the field in real space since at any rate we need to perform 13 inverse FFTs of the k -space field to generate the associated real-space fields (as explained below), so we would have saved only 7% of the CPU time associated with the FFTs.

2.2 Quasar generation

Quasars are biased tracers of the matter distribution and we wish to place quasars so that their power spectrum is close to the Kaiser power spectrum

$$P_{QSO}(\mathbf{k}, z) = b_{QSO}^2(z)(1 + \beta_{QSO}(z)\mu_k^2)^2 P_m(k, z), \quad (2.4)$$

where b_{QSO} and β_{QSO} are the quasar bias and RSD parameters, $\mu_k = k_{\parallel}/k$, and P_m is the matter power spectrum. In Refs. [27] and [30], candidates for quasar locations were uniformly drawn in cells where the matter field is above a given threshold, which is selected to produce the required bias. The selected peaks were then Poisson sampled to follow the observed quasar redshift distribution. Varying the threshold with redshift provides a z -dependent correlation function. As indicated by formula 5.102 in [37], this procedure works well when the correlation function is $\xi \ll 1$, i.e. on large scales, but on small scales it results in a quasar auto-correlation function that is significantly larger than the linear prediction, and also larger than the observed auto-correlation, as measured e.g. in Ref. [38].

To solve this problem, we used lognormal fields [39]. We produce a quasar-density box, filled with a Gaussian field δ_q which, like δ_m , is derived from the original $\hat{\delta}(\mathbf{k})$ but with mode amplitudes, $\hat{\delta}_q(\mathbf{k})$, that are modified from the $\hat{\delta}_m(\mathbf{k})$ of eqn 2.1: $\hat{\delta}_q(\mathbf{k}) = \sqrt{P_q(\mathbf{k})/V} \hat{\delta}(\mathbf{k})$ where $P_q(k)$ is the Fourier transform of $\ln[1 + b_{QSO}^2(z_0)\xi_m(r, z_0)]$. We then draw a quasar in each voxel with a probability proportional to the lognormal field, $\exp(\delta_q)$. Once a voxel is selected to host a quasar, the quasar position is drawn uniformly within the voxel, as in Refs. [27] and [30]. Ref. [39] showed that the correlation function of the lognormal field $\exp(\delta_q)$ has the form $b_{QSO}^2(z_0)\xi_m(r, z_0)$. The quasar velocity is taken from Eq. 2.2, yielding a redshift parameter $\beta_{QSO} = f/b_{QSO}$.

The quasar bias evolves with redshift as $b_{QSO}(z) = 3.7 \times ((1+z)/(1+2.33))^{1.7}$ [38]. The z -dependence of the quasar correlation function is implemented by producing three quasar-density boxes at $z_1 = 1.9$, $z_2 = 2.75$ and $z_3 = 3.6$ and interpolating between them, as described in appendix A.

2.3 Gaussian fields along lines of sight

We next define a Gaussian field, g , defined along lines of sight to quasars and subdivided into pixels of length $0.2 h^{-1} \text{Mpc}$. The field has three components:

$$g = \delta_L + \delta_S + c_{GP}(z)\eta_{\parallel}, \quad (2.5)$$

The components δ_L and η_{\parallel} describe the large-scale density and velocity-gradient fluctuations and are derived directly from the voxel values of δ_m and η_{pq} given by equations 2.1 and 2.3. The parameter $c_{GP} = \beta_{Ly\alpha}/f$ describes the desired RSD due to the bias parameter $\beta_{Ly\alpha}$ and growth rate $f \approx 1$. The component δ_S accounts for small-scale density fluctuations not included in δ_L .

If the values of δ_L and η_{\parallel} at each pixel were defined by the values of δ_m and η_{pq} at the nearest voxel, there would be discontinuities and then aliasing to small scales, i.e. spurious power on k larger than $k_N = \pi/a$ (Nyquist k), where a is the side of the box voxels. To avoid this, the value of the spectra in a given pixel is defined as a Gaussian-kernel average over neighboring voxels. We use the voxel side as the standard-deviation of this Gaussian smoothing, which cuts the power spectrum at large k , making the aliasing terms at $k > k_N$ completely negligible. In practice we compute the Gaussian weighting including three voxels in each direction, i.e. $7^3 = 343$ voxels, which means truncating the Gaussian at more than 3σ , which has negligible effect on the value of δ_L and η_{\parallel} .

The small effect of the Gaussian smoothing on the correlation function of δ_L can be computed and the even smaller effect of the averaging over voxel volumes can be approximated. For the nominal voxel size used, $a = 2.19 h^{-1}$ Mpc, the difference between the correlation functions of δ_L and matter on scales larger than about $10 h^{-1}$ Mpc is much less than the observational uncertainties for eBOSS final data (DR16).

While the δ_L pixels reflect the matter 3d correlation on large scales, the Mpc size of the voxels means that δ_L does not contain a significant amount of small scale fluctuations, as detailed in appendix B. This results in a pixel variance and a 1d power spectrum of the field that are significantly lower than in real data². Solving this issue by reducing the voxel size to the Jean’s scale would require 3d FFT with more than 10^{13} voxels, which is not feasible.

The idea is then to add a small scale spectrum to the large scale spectrum, $\delta = \delta_L + \delta_S$, where δ_S is a random spectrum that is generated independently for each spectrum. It is therefore uncorrelated between different lines-of-sight and the 3d correlation function of δ is then that of δ_L , keeping a 3d correlation function close to that of matter. We use the same procedure to generate the δ_S spectrum in 1d as was used to generate the δ_m box in 3d: a Gaussian field is defined over the pixel range, and the Fourier components of this field are multiplied by the square root of the desired 1d power spectrum. An inverse Fourier transform then defines δ_S . This allows us to give to δ_s the required 1d correlation on all scales to get a 1d power spectrum for the flux close to that of the data.

²The apparent contradiction between proper 3d correlation function and significantly smaller 1d power spectrum is discussed in the appendix.

2.4 FGPA

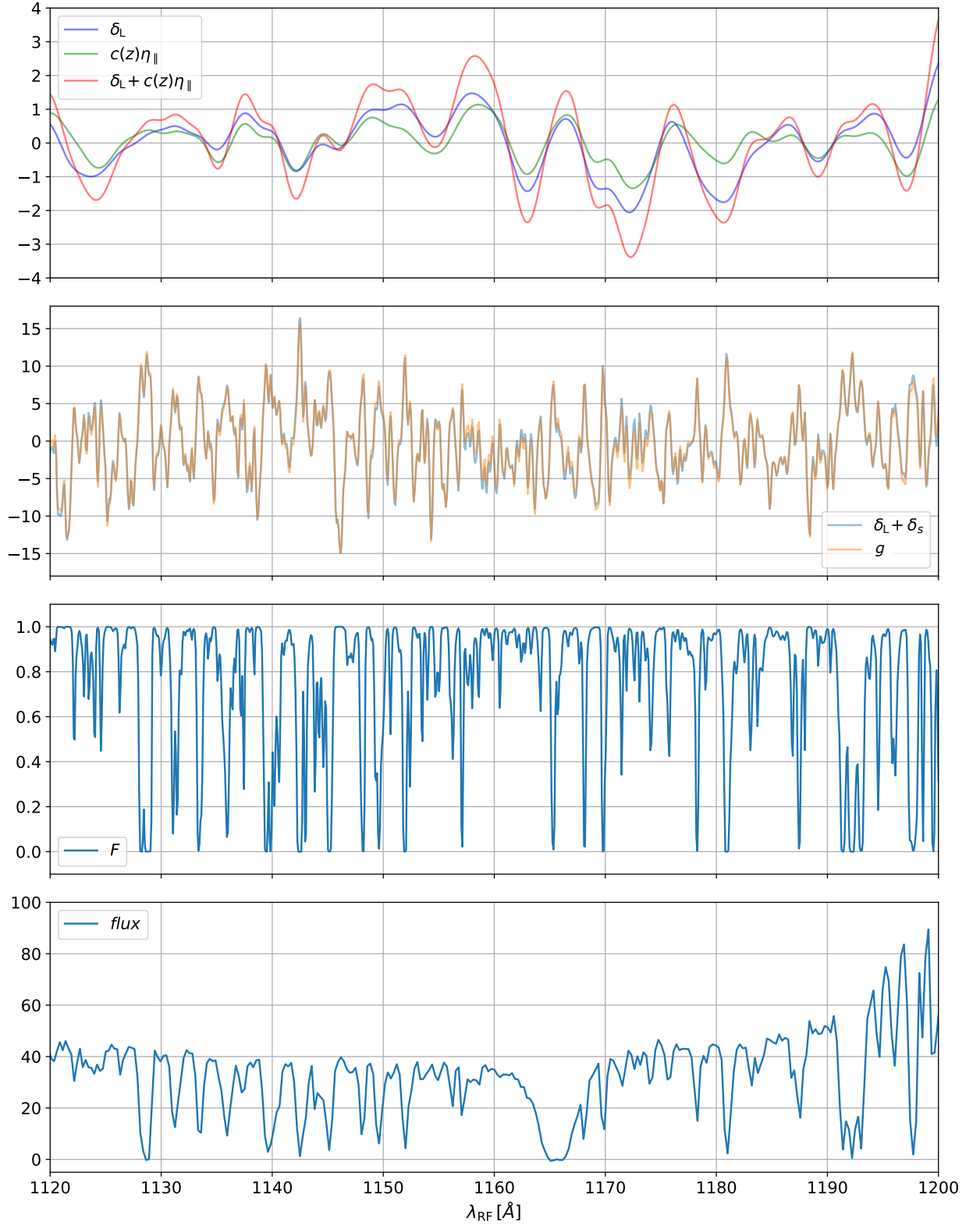


Figure 2. Steps in the production of mock forests showing for one representative forest the fields as a function of quasar restframe wavelength, λ_{RF} . From top to bottom, the first graph shows the large-scale fields δ_L , $c(z)\eta_{\parallel}$ and the sum of the two. The second presents the sum $\delta_L + \delta_S$ and the field $g = \delta_L + \delta_S + c(z)\eta_{\parallel}$. The third presents the transmitted flux fraction F , and the last graph presents the spectrum (the product of F and the unabsorbed quasar spectrum). A DLA has been added at $\lambda_{\text{RF}} \approx 1165 \text{\AA}$.

The basic idea behind the FGPA is that the optical depth for Ly α absorption by the IGM is $\tau(z) \propto n_{\text{HI}}(z)/v'(z)$, where n_{HI} and v' are the neutral hydrogen density and velocity gradient at the redshift where photons of a given observed wavelength can induce the Ly α transition [40]. This formula is valid if when thermal broadening and turbulence can be neglected as indicated by hydrodynamical simulations of the IGM. In addition, the simple physics that governs the ionization of the low density intergalactic medium implies that $n_{\text{HI}} \propto (1+\delta)^b$ [41]. If one neglects peculiar velocity fluctuations, the lognormal approximation [39, 42] then leads to $\tau \propto \exp(b\delta)$, and the more readily measured transmitted flux fraction is $F = \exp(-\tau) = \exp[-a \exp(b\delta)]$ ³

Including line-of-sight velocity gradient fluctuations, η_{\parallel} , within the lognormal approximation defines F in terms of the Gaussian field $g(\lambda)$ (eqn. 2.5):

$$F(\lambda) = \exp[-a_{\text{GP}}(z) \exp(b_{\text{GP}}(z)g)] \quad \text{with} \quad g(\lambda) = \delta_L(\lambda) + \delta_S(\lambda) + c_{\text{GP}}(z)\eta_{\parallel}(\lambda), \quad (2.6)$$

The additional bias redshift-dependent parameter, c_{GP} , would be a simple function of the mean flux [43, 44] were it not for residual thermal effects. We treat it, along with a_{GP} , b_{GP} and the power spectrum of δ_S , as parameters that are chosen to reproduce the observed statistical properties of F , as described in Sect. 2.6. For the wavelength λ associated with the line-of-sight pixels, we use the unperturbed cosmological redshift, i.e. we neglect the peculiar velocity in the wavelength calculation. Mathematically, this ensures that the power spectrum of the g field corresponds to the Kaiser formula (see section 2.5). Including the peculiar velocity in the wavelength calculation would result in a slightly different power spectrum.

Fig. 2 gives an example of a spectrum, with the different steps from δ_L to F .

We emphasize that while there is some physical justification of eqn. (2.6), it should be just considered as a convenient way of generating mocks with the appropriate correlations.

2.5 The expected auto-correlation function of the mocks

Our implementation of RSD differs from Refs. [27] and [30], which used the FGPA without velocity gradient fluctuations and then introduced the RSD by displacing the HI according to the peculiar velocity. Our introduction of the velocity gradient directly in the FGPA has the nice feature that it allows us to predict the correlation function of the mocks. In this section we discuss this prediction, given the mock parameters and in particular the FGPA transformation.

Since the field δ_S is generated independently for each spectrum, the 3d correlation of δ_S vanishes, and including δ_S in the field $g = \delta_L + \delta_S + c_{\text{GP}}(z)\eta_{\parallel}$ does not change its 3d correlation, it only adds noise. Eq. 2.3 implies that $\hat{\eta}_{\parallel} = f[(\mathbf{u} \cdot \mathbf{k})^2/k^2]\hat{\delta} = f\mu_k^2\hat{\delta}$ and the power spectrum of the field g is, ignoring the noise from δ_S

$$P_g(\mathbf{k}) = (1 + f c_{\text{GP}} \mu_k^2)^2 \times P_m(k, z=0) W^2(\mathbf{k}), \quad (2.7)$$

where the window $W(\mathbf{k})$ is the product of a Gaussian smearing window (with standard deviation $1/a$) and the three windows that take into account the averaging of the field over the cubic voxels in the three directions, e.g. $W_x = \text{sinc}(k_x a/2)$, where $a = 2.19h^{-1}$ Mpc is the voxel side. Replacing the product $W_x W_y W_z$ by the window of a sphere of diameter a (that is entirely inside the voxel)⁴ results in an overestimation of the product, while a sphere of diameter $\sqrt{3}a$ (that includes the whole voxel) results in an underestimation. We use the approximation $W_x W_y W_z \approx \text{sinc}^3(ka/(2\sqrt{3}))$, where we assume that in average $k_x = k_y = k_z = k/\sqrt{3}$, which nicely sits between the under- and over-estimation. This approximation depends only on k and can be

³this is also sometimes referred to as the FGPA, e.g. Eq 2.5 in Ref. [30].

⁴The window is $3(\sin x - x \cos x)/x^3$ with $x = ka/2$

included in the definition of the power spectrum. Eq. 2.7 then corresponds to a Kaiser power spectrum with RSD parameter $\beta = fc_{\text{GP}}$ and the correlation function of g can be obtained using formulas (5) to (9) of Ref. [45]. It appears that the dominant window effect is the Gaussian one and the choice of the approximation for $W_x W_y W_z$ does not really matter. (Fig. 18 of Appendix B illustrates this for the case of P^{1d} .)

The correlation function of F is then deduced from that of g using Eqn. (2.6) of ref. [25]. In Sect. 4.2 (Fig. 5), we will see that the prediction is correct to a good approximation, even if there is a small discrepancy along the line-of-sight, which we ascribe to our approximation for the product $W_x W_y W_z$. In the range where we usually fit the data, $r > 20h^{-1}$ Mpc, the prediction agrees with the measurement within the error of one realization of eBOSS.

2.6 Adjusting mock parameters

To produce mocks with the desired properties, parameter tuning is performed for 5 values of the redshift, $z_t = 1.8, 2.2, 2.6, 3.0$ and 3.6 , and then interpolated for other values of z . At a given z_t , the mock parameters include $a_{\text{GP}}(z_t)$, $b_{\text{GP}}(z_t)$ and $c_{\text{GP}}(z_t)$ that appear in Eq. 2.6 and the power spectrum, $P_s(k, z_t)$, of the field δ_S over the range $[0, 2] h\text{Mpc}^{-1}$. The values of these parameters are chosen to produce the desired values of the mean transmitted flux fraction $\bar{F}(z)$, a 3d power spectrum that is a Kaiser power spectrum with bias parameters, $b_{\text{Ly}\alpha}(z)$ and $\beta_{\text{Ly}\alpha}(z)$, and a 1d flux power spectrum, P_f^{1d} , as measured by BOSS [46]. We will see that the tuning procedure succeeds in producing physically reasonable mocks while not yielding exactly the target parameters and correlations.

In practice, instead of targeting a value of $b_{\text{Ly}\alpha}$ for each z_t we target an effective bias, $b_{\text{eff,Ly}\alpha} = b_{\text{Ly}\alpha}(1 + 2\beta_{\text{Ly}\alpha}/3 + \beta_{\text{Ly}\alpha}^2/5)^{1/2}$, which is proportional to the monopole of the correlation function [45]. To choose the target values we analyzed the eBOSS DR16 data following the same procedure as Ref. [13]. We found that the bias parameters are well fit by power laws $b_{\text{eff,Ly}\alpha}(z) = 0.183[(1+z)/3.3]^{3.47}$ and $\beta_{\text{Ly}\alpha}(z) = 1.76[(1+z)/3.3]^{-2.32}$ (Fig. 6 of Sect. 4.2). We take these power laws as our targets.

For the mean transmitted flux fraction we use as target $\bar{F}(z) = \exp(-0.0028(1+z)^{3.45})$, which is the parameterization of the measured $\bar{F}(z)$ obtained by [47].

As already noted the RSD parameter of the g field is simply $fc_{\text{GP}}(z_t) = \beta_{\text{Ly}\alpha}(z_t)$. Given that g in eq. 2.6 is a Gaussian field (of variance σ_g^2), the values of \bar{F} and its variance σ_F^2 only depend on a_{GP} and $\sigma(b_{\text{GP}}g) = b_{\text{GP}}\sigma_g$ [25]. Therefore, we fit⁵ a_{GP} and $b_{\text{GP}}\sigma_g$ to reach the target $\bar{F}(z_t)$ and $\sigma_F(z_t)$, where the target for $\sigma_F(z_t)$ is obtained from the integral of our target $P_f^{1d}(k, z_t)$.

To fix $P_s(k)$, we use an iterative procedure. As an initial $P_s(k)$ we take the difference between the CAMB matter 1d power spectrum and the 1d power spectrum of the $\delta_L + c_{\text{GP}}\eta_{\parallel}$ field. (While this is a crude approximation since the CAMB spectrum ignores small-scale effects, it is sufficient as an initial spectrum.) The integral of this initial $P_s(k)$ gives σ_s (the dispersion of the field δ_s). We can measure σ_L , σ_{η} and $\text{cov}(\delta_L, \eta_{\parallel})$ directly on the produced boxes. We, therefore, have all elements to compute $\sigma_g^2 = \sigma_L^2 + \sigma_s^2 + c_{\text{GP}}^2\sigma_{\eta}^2 + 2c_{\text{GP}}\text{cov}(\delta_L, \eta_{\parallel})$. Since we already fixed the value of $b_{\text{GP}}\sigma_g$, this provides us with the value of b_{GP} . We can then generate spectra using this $P_s(k)$ and FGPA (Eq. 2.6) and compute the resulting P_f^{1d} . In each bin in k , P_s at iteration $n+1$ is defined from iteration n as $P_s^{n+1}(k) = P_s^n(k) \times (P_{\text{target}}(k)/P_f^{1d}(k))$. We stop after ten iterations, which provides a good agreement for P_f^{1d} .

However, the correlation function prediction (section 2.5) for these selected values of the mock parameters implies a bias that is a bit larger than our target. This might be do to the

⁵We use the Minuit package [48]

fact that the measured P_f^{1d} includes the HCD contribution, which increases the amplitude of the correlation function. We therefore make small adjustments of a_{GP} and b_{GP} to get a better value of the bias and keep a good value of \bar{F} , and perform again the previous procedure for $P_s(k)$.

After five iterations there is fair agreement for all parameters, as illustrated in Fig. 3 for \bar{F} , in Fig. 4 for $P^{1d}(k_{\parallel})$, and in Figs. 5 and 6 of Sect. 4.2 for the bias parameters and overall correlation function. For \bar{F} , the mocks have $\approx 1\%$ excess transmission at low redshift and a small excess at high redshift. For P^{1d} , Fig. 4 shows that the mocks have $\approx 10\%$ too much power for $z > 3.1$ and $\approx 10\%$ too little for $z < 2.1$. This has little impact on the correlation functions because there are few forest pairs with $z > 3.1$ and the flux fluctuations for $z < 2.1$ are dominated by instrumental noise. Figure 6 shows that the raw mocks reproduce the targeted bias parameters at the percent level. However, Fig. 5 shows noticeable differences in target and returned correlations for separations near the line of sight ($\mu > 0.95$). Finally, we note that the bias parameters found for the quasar-forest cross-correlations, as shown in Table 3 differ by of order 10% from those found for the auto-correlations.

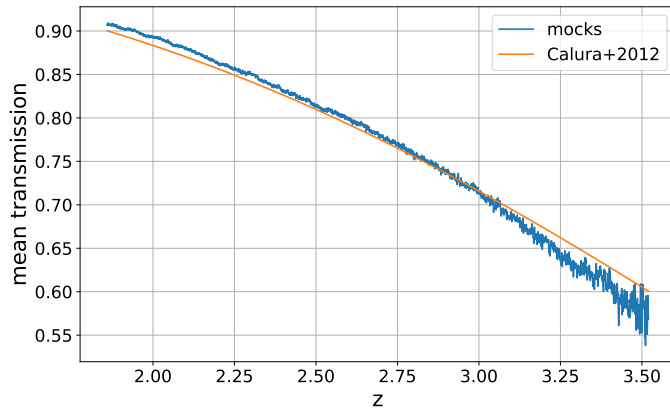


Figure 3. Mean transmitted flux fraction versus redshift, $\bar{F}(z)$. The blue curve is $\bar{F}(z)$ as measured on the mocks in the region $91.2 < \lambda_{\text{RF}} < 120$ nm, while the orange line is the parameterization of published data by Ref. [47].

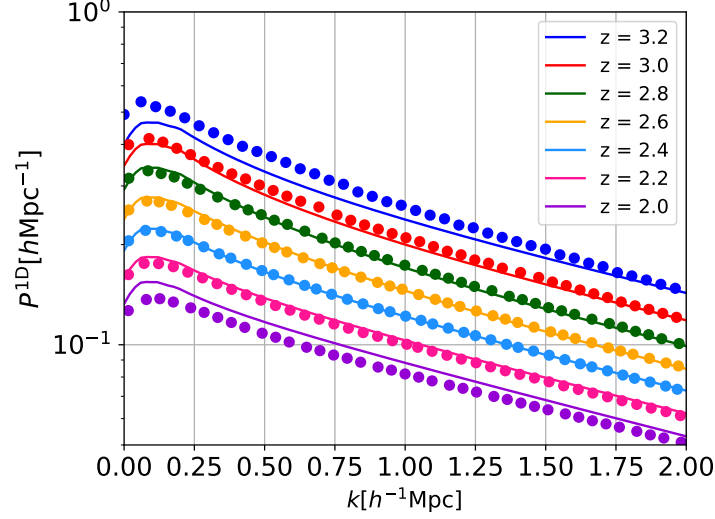


Figure 4. The measured 1d power spectrum, P_f^{1d} , of the mock data in bins in redshift compared to the target 1d power spectrum.

2.7 High column density systems (HCD)

The Ly α absorption in the IGM is responsible for most forest absorption but the production of realistic mocks requires the addition of other types of absorption in the post-production stages described in [33]. One type is absorption due to high column density systems (HCDs), i.e. condensed systems with neutral-hydrogen column-density $N(\text{HI}) > 10^{17.2}\text{cm}^{-2}$. HCDs with column density $> 10^{20.3}\text{cm}^{-2}$ are called damped Ly α systems (DLAs) and can be identified in eBOSS or DESI spectra of moderate signal to noise. About 6% of such spectra contain a DLA[31].

Like IGM absorption, absorption by HCDs is dominated by Ly α absorption but is spread out along the line of sight because of the system’s absorption profile. This modifies the flux correlation function by suppressing high- k modes along the line of sight [49]. For instance, a DLA of column density of $10^{20.3}\text{cm}^{-2}$ will entirely absorb the flux over a wavelength range corresponding to a comoving distance of $\approx 5h^{-1}\text{Mpc}$. The modeling of this effect in eBOSS and DESI spectra will be studied in a forthcoming publication [Tan et al, in preparation]. The eBOSS and DESI analysis pipelines mask the highly absorbed regions around detected DLAs so one needs only model the effect of HCDs that are undetected, either because their column density is too small ($< 10^{20.3}\text{cm}^{-2}$) or because they are in low signal-to-noise forests. The current modeling of HCDs in DESI involves two parameters, one giving the strength of HCD absorption and a second giving the length scale of the most important absorbers.

In order to include HCDs in the second stage of mock production, the first stage produces a catalog of possible HCD positions is selected from peaks of the large-scale density field, δ_L , with the threshold set so as to produce a redshift-independent HCD bias $b_{\text{HCD}}(z) = 2$ [16]. The threshold is set using an analytic evaluation of eqn. A2 in appendix A of Ref. [50]. The selected peaks are then Poisson sampled to follow the HCD redshift distribution of the default model from the IGM physics package pyigm⁶ [51], which is fitted to a selection of literature results, summarised in table 1 of Ref. [52]. Then a column density is randomly ascribed to each HCD to follow the column density distribution of the same model. The radial velocity of the HCD is

⁶<https://github.com/pyigm/pyigm>

obtained from the three velocity-component boxes, as for the quasars.

Our implementation of HCDs is clearly approximate because there are no measurements of the number or bias of HCDs in the range $10^{18} < N(\text{HI}) < 10^{20} \text{cm}^{-2}$. We can expect, however, that the most important HCD effects on the correlation function come from the unmasked HCDs with the highest column density, near $N(\text{HI}) \approx 10^{20}$ where the extrapolation of the measurements should be reliable.

2.8 Metals

The other major secondary source absorption is that due to non-HI species, i.e. metals, either in the IGM or in condensed systems. The presence of such absorption complicates the modeling of the $\text{Ly}\alpha$ forest correlations because the transformation of wavelengths to comoving radial distances necessarily assumes that features are due to $\text{Ly}\alpha$ absorption. The presence of metallic absorption and its correlation with $\text{Ly}\alpha$ absorption results in "phantom" correlations superimposed on the physical correlation function but shifted in the radial direction. This effect is simple to model as described in Sect. 4 of [13]. Because of their proximity to the $\text{Ly}\alpha$ wavelength, the most important metallic species are four silicon transitions: SiII(1190), SiII(1193), SiII(1260), and SiIII(1207).

The procedure for adding metallic absorption in the post-production stage is described in [33]. The currently used process assumes that absorption by metals are proportional to that by HI and follows the same procedure as the eBOSS mocks described in Farr et al. [30]. An alternative procedure, proposed by [30], would be to place the metals in density peaks as is done for quasars and HCDs.

3 Implementation and production

The code was run at National Energy Research Scientific Computing Center (NERSC) on Cori machines without requiring the use of different nodes in parallel. The nodes of this machine have 64 threads and 128 Gb memory, which limits the number of voxels of the boxes. We have used boxes with $2560 \times 2560 \times 1536$ cubic voxels of $2.19 h^{-1} \text{Mpc}$ side. One such box is not enough to cover neither the north galactic cap (NGC) nor the south one (SGC) of the eBOSS or DESI footprints and we use five boxes for the NGC and two boxes for the SGC as illustrated by Fig. 1. This means that there is no correlation between spectra produced in different chunks. However if we consider separation below $200 h^{-1} \text{Mpc}$, the proportion of pixel pairs with pixels that belong to different chunks is negligible.

The code is written in python and is available on github⁷. For one realization of the mocks we must produce 7 independent chunks, which we finally merge. The procedure consists of four steps summarized in Table 2. First, the module `make_box.py` produces the 13 boxes for the considered chunk (1 density box, 3 lognormal density boxes, 3 velocity boxes and 6 velocity gradient boxes). This module was run using one Cori node, taking advantage of the pyFFTW⁸ package to run the FFT in parallel on the 64 threads of the node. The module `draw_qso.py` then samples the box to draw quasars, as described in section 2.2 and the module `make_spectra.py` computes the density along each line-of-sight. These two modules run on 512 threads over 16 nodes. The box is split into 512 slices along a direction perpendicular to the line-of-sight and each thread treats one slice. This constitutes the “pre-production” of the realization. This is where we have strong constraints in terms of CPU consumption and, in the case of `make_box.py`, in terms of memory.

⁷<https://github.com/igmhub/SaclayMocks>

⁸<https://github.com/pyFFTW/pyFFTW> based on FFTW library, <http://www.fftw.org>

Table 2. CPU and memory requirements for mock production. Columns 2, 3 and 4 give requirements for one chunk and column 5 gives the requirement for a complete realization of 7 chunks on Cori.

	1 chunk			1 realization
	time (min)	node (64 threads)	memory (Gb)	time \times thread (h)
<code>make_box.py</code>	210	1	120	1570
<code>draw_qso.py</code>	2	16	not critical	240
<code>make_spectra.py</code>	6	16	not critical	720
<code>merge_spectra.py</code>	3	16	not critical	360

The second step is the “post-production”, which involves combining the pieces of spectra from the different slices of the box, adding small-scale field, δ_S , and applying the FGPA (`merge_spectra.py`). This produces a set of "transmission files" containing for each line-of-sight, q , the transmitted-flux fraction $F_q(\lambda)$. A catalog of HCD is also produced which, if desired, can be added to the $F_q(\lambda)$ at a later stage.

After the production of the transmission files following the steps of Table 2, the final step of the mock production samples the set of transmission files to provide the desired density of quasars ($\approx 20\text{deg}^{-2}$ for eBOSS up to $\approx 100\text{deg}^{-2}$ for DESI) and then transforms the transmission-fractions $F_q(\lambda)$ into fluxes, $f_q(\lambda)$. This is done with a script named `quickquasars`⁹, which is a compilation of DESI code within the `desisim` package¹⁰, as described in Section 2.2 of [33]. It multiplies the $F_q(\lambda)$ by quasar continua chosen from a library of realistic quasar spectra [53]. Instrumental noise is also added at this stage. Options for `desisim` include multiplication by Voigt profiles due to HCDs and the addition of absorption by metals. The produced spectra files in the same format as real data.

In what follows, the set of $F_q(\lambda)$ obtained before applying `desisim` are referred to as "raw" mocks. The set of fluxes $f_q(\lambda)$ obtained by `desisim` are referred to as "cooked" mocks.

Table 2 presents the CPU and memory requirements for the different modules of the production of the transmission files. The first three lines are the main parts of the pre-production, which requires a total time of about $2500 \text{ h} \times \text{threads}$ of CPU. The last line is `merge_spectra.py`, which dominates the post-production and requires about $350 \text{ h} \times \text{threads}$, and does not have significant memory requirements. So the post-production can be run easily.

A hundred sets of transmission files have been produced. The output of the pre-production are saved so that if we decide to change the parameters of the mocks that enter eq. 2.6, we only have to re-run the post-production, which does not require important memory or CPU resources.

4 Analysis of the mock data sets

The mock data sets consist of a set of Ly α forests and sets of two types of discrete objects, quasars and HCDs. To verify that the sets have the expected characteristics, we studied three types of correlations: forest-forest auto-correlations; forest-quasar cross correlations; and quasar-quasar auto-correlations. (Correlations with HCDs will be studied in [Tan et al, in preparation]) In this section, we first describe the analysis procedure and then present the correlation functions measured for raw and cooked mocks with eBOSS quasar densities ($\approx 20\text{deg}^{-2}$) and noise. We then give the results of fits of the correlations to a Λ CDM-based model, as summarized in Table 3.

⁹<https://github.com/desihub/desisim/blob/main/py/desisim/scripts/quickquasars.py>

¹⁰<https://github.com/desihub/desisim>

4.1 Analysis procedure of forest correlations

Correlations involving the forests were analyzed using the standard eBOSS and DESI pipeline, `picca`¹¹, which is described for instance in Ref. [13]. The main steps are as follows:

1. Calculation of the flux-transmission field, $\delta_q(\lambda)$, for each quasar, q . The calculations uses the flux $f_q(\lambda)$ (for the cooked mocks), or the transmission, $F_q(\lambda)$ (for the raw mocks):

$$\delta_q(\lambda) = \frac{f_q(\lambda)}{\overline{F}(\lambda)C_q(\lambda)} - 1. \quad \text{or} \quad \delta_q(\lambda) = \frac{F_q(\lambda)}{\overline{F}(\lambda)} - 1. \quad (4.1)$$

Here $\overline{F}(\lambda)$ is the mean transmitted flux fraction and $C_q(\lambda)$ is the estimated unabsorbed quasar continuum. We calculate the $\delta_q(\lambda)$ in a wavelength range between the Ly α and Ly β quasar lines: $1040 < \lambda_{\text{RF}} < 1200\text{\AA}$.

In the standard analysis of the cooked mocks or of data (Sect. 2.4 of [13]) the product $\overline{F}(\lambda)C_q(\lambda)$ is determined by fitting each forest to the mean forest spectrum modified by two free parameters per quasar reflecting the quasar brightness and spectral index. Such a simple procedure does not fully take into account the peculiar features of individual quasar spectra. Fortunately, the sources of quasar spectral diversity are believed to be due to astrophysical conditions near the quasar and are therefore unlikely to lead to correlated absorption in forests separated by cosmological distances.

For the raw analysis, the mean transmission $\overline{F}(\lambda)$ (Fig. 3) can be estimated by averaging the transmission $F_q(\lambda)$ over all forests, q , in small wavelength ranges. However, because these F_q are all near a host quasar, they are not a representative sample of the whole IGM, and the correlation with the host results in a slight underestimation of \overline{F} of $\approx 10^{-4}$. (see Sect. 4.2). An unbiased value $\overline{F}(\lambda)$ could be measured on lines-of-sight that were randomly selected rather than being required to be in front of quasars. Lacking such data, we added a constant to the \overline{F} so that the mean $\delta_q(\lambda)$ far in front of the quasars had the expected value of the cross-correlation at $r \approx 200h^{-1}\text{Mpc}$. (See Fig. 7) This small shift has negligible effect on the best-fit model parameters.

2. Use of the fiducial cosmological model used to construct the mocks to transform forest-pixel pair separations or quasar-pixel separations $(\Delta z, \Delta\theta)$ into co-moving distances (r_\perp, r_\parallel) (Sect. 3.1 of [13])
3. Calculation of the forest auto correlation function and quasar-forest cross correlation in bins $\Delta r_\perp = \Delta r_\parallel = 4h^{-1}\text{Mpc}$ (Sections 3.2 and 3.3 of [13]):

$$\xi_A^{\text{auto}} = \frac{\sum_{(i,j) \in A} w_i w_j \delta_i \delta_j}{\sum_{(i,j) \in A} w_i w_j} \quad \xi_A^{\text{cross}} = \frac{\sum_{(i,q) \in A} w_q w_i \delta_i}{\sum_{(i,q) \in A} w_q w_i}. \quad (4.2)$$

For the auto-correlation, the sum is over pixel pairs in the (r_\perp, r_\parallel) bin A and the w_i are weights chosen to optimize the measurement. For the cross correlation, the sum is over quasar pixel pairs.

4. Calculation of the covariance matrix of the auto- and cross-correlations by subsampling (Sections 3.2 and 3.3 of [13]). The method consists of measuring the correlation functions in different regions of the sky and deducing the covariances from the variations between different regions.

¹¹<https://github.com/igmhub/picca>

5. Fit of the measured ξ with a Λ CDM-based model (Sect. 4 of [13]).

The model used to fit the correlations is based on the Λ CDM power spectrum modified to allow for a change in the position of the BAO peak with respect to the fiducial model and by Kaiser factors to describe biasing and RSD.

The parameters of the fits are listed in Table 3.. The two parameters $(\alpha_{\perp}, \alpha_{\parallel})$ describe the position of the BAO peak. The density and velocity biases, $(b_{Ly\alpha}, b_{\eta Ly\alpha})$ are related by the fit parameter $\beta_{Ly\alpha} = f b_{\eta Ly\alpha} / b_{Ly\alpha}$, where $f \approx 1$ is the growth rate at $z \approx 2.3$.

Fits for the quasar-forest cross-correlation include a parameter, Δr_{\parallel} , that, for real data, compensates for systematic errors in quasar redshift estimation. We include it in the fit of the mock data, yielding, as expected, a value consistent with zero. The values of b_{QSO} and β_{QSO} for these fits are fixed to the values determined for the quasar auto-correlation (Sect. 4.4).

For cooked mocks and for data, the model correlation and cross-correlations functions must be multiplied by a “distortion matrix” which corrects for the effect of the continuum fitting used in step 1 for the cooked mocks (Sect. 3.5 of [13]).

4.2 Forest correlations in the raw mocks

The raw mocks were analyzed using the second form of eqn. 4.1 to define the flux-transmission field. The aim was first to verify that the produced forest-forest auto-correlations corresponded well to the expectations defined in Sec. 2.5. Second, we investigated the extent to which the forest-quasar cross-correlation was correctly predicted by the same model as that for the auto-correlation.

The $Ly\alpha$ auto-correlation was computed for 30 raw mock realizations of the eBOSS footprint and quasar density. The correlations were calculated for the entirety of the data, corresponding to a mean pixel-pair redshift $z_{eff} = 2.261$. The correlations were also calculated in four redshift bins of similar statistics. Following [8] redshift bins were defined by the mean quasar redshift of all pairs of forests. Ranges for the mean quasar redshift were defined: $2.0 < z < 2.35$; $2.35 < z < 2.65$; $2.65 < z < 3.05$ and $z > 3.05$. All forest-pixel pairs of the forest pairs were used to calculate the auto-correlation for that range. This led to measurements for the z_{eff} values 2.101, 2.237, 2.542, and 2.866.

The results of fits to the correlations for the stack of 30 mocks are presented in Fig. 5. In each redshift bin the correlation function is shown in 4 bins in $\mu = r_{\parallel}/r$. The dashed curve is the prediction (section 2.5), which is fairly good, with only some disagreement at low r in particular near the line-of-sight ($0.95 < \mu < 1$). The continuous line is the fit of the mock data with the picca model, it is in good agreement even at low r . The χ^2 are 1557, 1608, 1628 and 1534 in the 4 bins in redshift for 1570 degrees of freedom.

In Fig. 6 the red points show $b_{eff, Ly\alpha}$ and $\beta_{Ly\alpha}$ measured in the raw mocks in four redshift bins for the average of 30 raw mock realizations. The figure also shows the same quantities for DR16 data together with power law fits to them, which were used as input parameterization for the mocks. We note that the values obtained for the raw mocks are consistent with those of the DR16 data. Due to the small error bars obtained on the mocks we can see a small disagreement with the fit in the case of $\beta_{Ly\alpha}$ at low z . This level of disagreement is much lower than the error bar of the data.

We next studied the raw forest-quasar cross-correlations. They were not used to tune the mocks and, as such, their measurement in the mocks is a consistency check to determine to what extent the auto-correlation and cross-correlation can be described by the same model.

We first studied the cross-correlations between a quasar and its own forest, i.e., $\xi(\mu = 1)$ given by the mean flux-transmission in front of a quasar. This correlation cannot be measured

Table 3. Best-fit parameters for stacks of 30 eBOSS mocks over the entire mock redshift range. Results are shown for the raw and cooked auto-correlation function (CF) and cross-correlation function (XCF). The first four rows show the best-fit χ^2 for the fit with N_{data} (r_{\perp}, r_{\parallel}) bins with N_{par} free parameters, leading to a χ^2 probability P . The next rows give the best-fit parameters values for $(\alpha_{\parallel}, \alpha_{\perp}, b_{\eta}, \beta)$ and Δz_{\parallel} for the XCF, and the derived parameters b_{eff} . The target values used to tune the mocks are shown for $\beta(z_{eff})$ and $b_{eff}(z_{eff})$ for the mean redshift of the measurement, z_{eff}

	raw CF	cooked CF	raw XCF	cooked XCF
χ^2	1676.07	1562.54	3454.94	3502.09
N_{data}	1574	1574	3148	3148
N_{par}	4	4	5	5
P	0.031	0.548	0.0	0.0
α_{\parallel}	1.001 ± 0.003	1.003 ± 0.005	1.002 ± 0.004	0.999 ± 0.005
α_{\perp}	0.995 ± 0.004	0.995 ± 0.008	1.000 ± 0.004	1.0 ± 0.006
$-b_{\eta}$	0.196 ± 0.0003	0.2077 ± 0.0005	0.1754 ± 0.0006	0.1902 ± 0.001
β	1.804 ± 0.007	1.687 ± 0.008	1.583 ± 0.011	1.564 ± 0.015
(target)	1.809	1.774	1.782	1.758
Δr_{\parallel} ($h^{-1}\text{Mpc}$)			0.013 ± 0.026	-0.033 ± 0.035
b_{eff}	0.1835 ± 0.0002	0.2021 ± 0.0003	0.1772 ± 0.0004	0.1935 ± 0.0006
(target)	0.1756	0.1807	0.1795	0.1831
z_{eff}	2.261	2.288	2.282	2.301

in the standard analysis of the cooked mocks (nor in the data) because the correlation affects the forest flux in front of the host quasar and is therefore absorbed into the continuum template. We can measure the correlation with the raw mocks because the mean transmission, $\bar{F}(z)$ can be determined, as explained in Sect. 4.1, by averaging the $F_q(\lambda)$ over all lines-of-sight and then correcting for the slight underestimation caused by the correlation with the host quasar.

The $\mu = 1$ cross correlation is shown in the left plot of Fig. 7. The correlation is $\approx 2 \times 10^{-3}$ at a separation of $40h^{-1}\text{Mpc}$ corresponding to the point in the forest nearest the host quasar. The correlation then drops off to $\approx 10^{-4}$ far in front of the quasar. The mean of $\delta_q(\lambda)$ in the forest is $\approx 2 \times 10^{-4}$.

The $\mu \neq 1$ cross-correlation in four ranges of μ is shown in the right plot of Fig. 7. The best-fit model shows non-negligible deviations from the measurements. Figure 8 gives the best-fit bias parameters as a function of redshift. We see that the effective bias is in good agreement with the expected value at all redshift while β is about 10% lower than expectations.

The $\mu = 1$ cross-correlation shown in the left panel of Figure 7 indicates to what extent the forests in front of a quasar do not represent a random sample of the IGM. By definition, the mean δ in the IGM vanishes, whereas the mean δ in the observed forest $\approx 2 \times 10^{-4}$. This has little effect on the auto correlations (order δ^2) but means that extraction of the cross correlation in the raw mocks is significantly biased wherever the correlation is less than 10^{-3} . It is then not surprising that the fits of the raw mocks give cross-correlation values of bias parameters (Fig. 8) that agree with expectations only at the 10% level. Fortunately, this issue has no observable effect on the BAO parameters shown in Table 3.

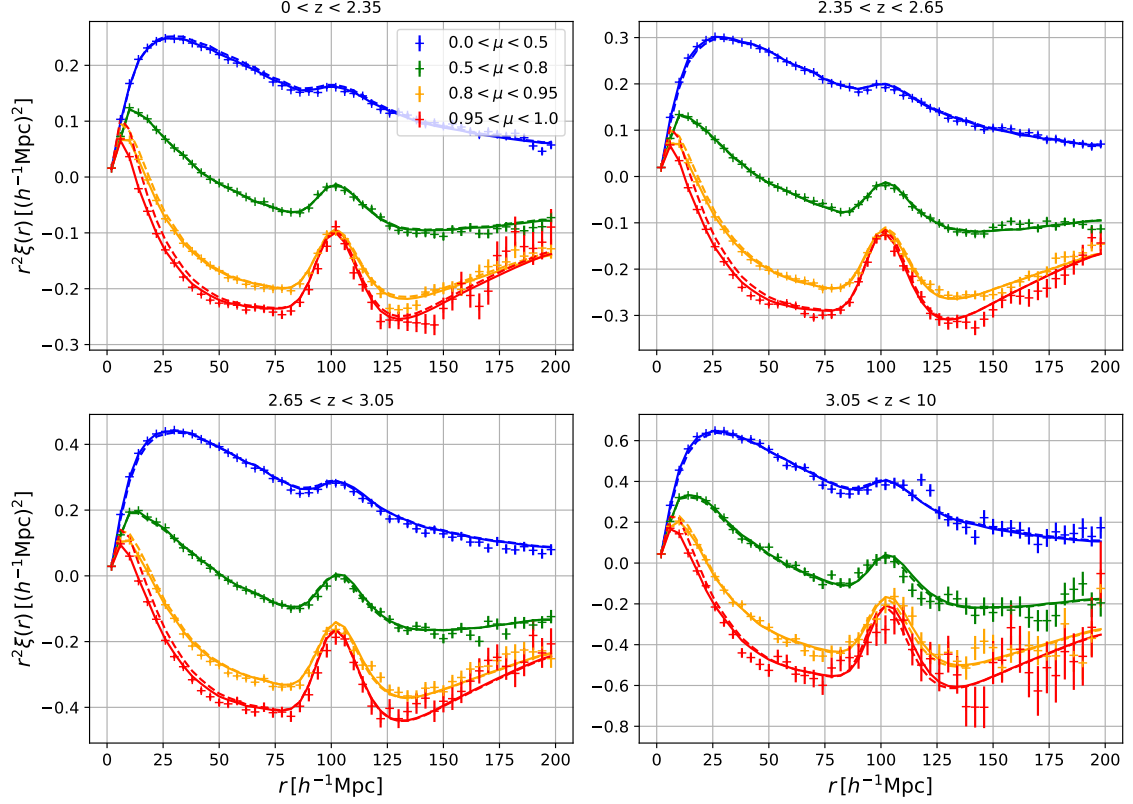


Figure 5. Ly α auto-correlation of 30 raw mock realizations. The four panels correspond to different bins in redshift. Each one gives the average of the correlation functions calculated for the 30 realizations. The correlation functions are presented in four bins in μ . The continuous lines give the fit by picca model and the dashed lines the prediction (section 2.5).

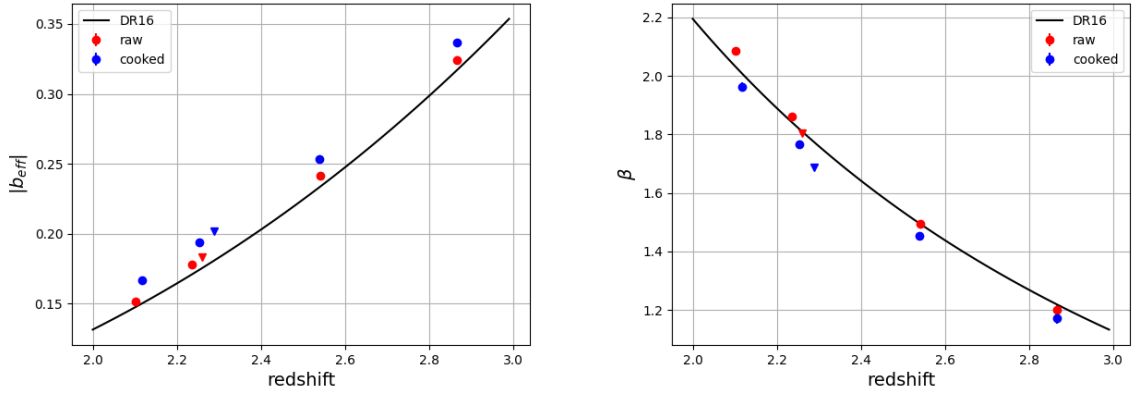


Figure 6. Ly α auto-correlation: the effective bias (left) and the RSD parameter (right) as a function of redshift. The red points are for the raw mocks and the blue points for the cooked mocks. The triangles are for the fit over all redshifts (Table 3) The black lines are fits to the DR16 auto-correlation, that were used as the targets of the mocks

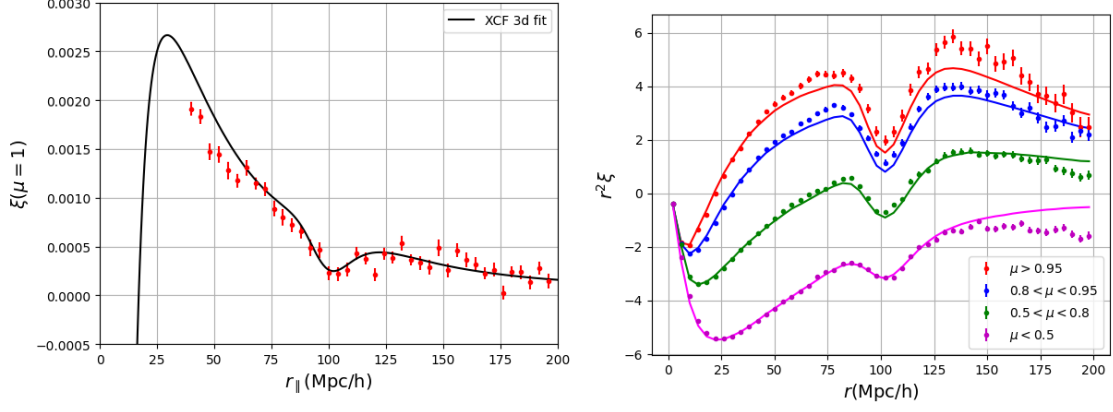


Figure 7. Raw cross-correlation between host quasars and their forest (left) and the raw 3d cross-correlation in different μ ranges (right). The solid lines show that best fits to the raw 3d cross-correlation (Table 3)

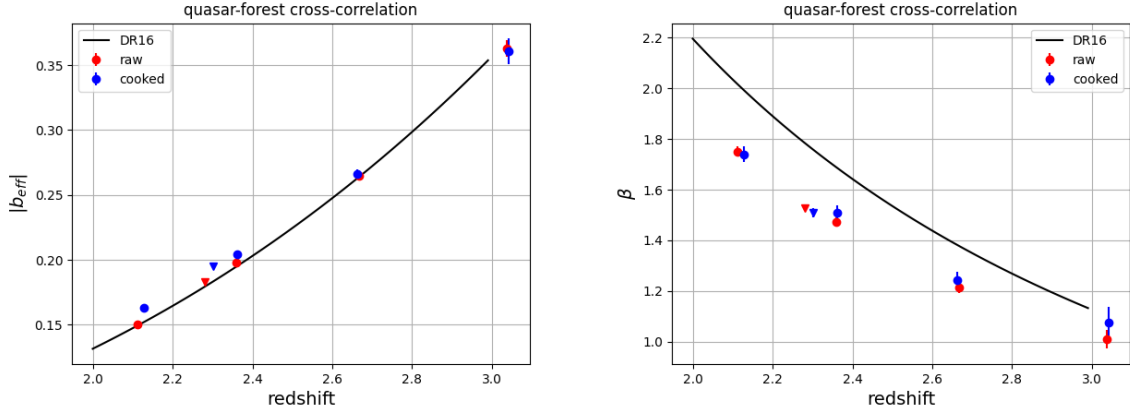


Figure 8. Same as Fig. 6 except now for the quasar- $\text{Ly}\alpha$ cross-correlation: the effective bias (left) and the RSD parameter (right) as a function of redshift, calculating assuming the quasar bias of [38]. The red points are for the raw mocks and the blue points for the cooked mocks. The triangles are for the fit over all redshifts (Table 3) The black line is a fit to the DR16 auto-correlation.

4.3 Forest correlations in the cooked mocks

We now consider cooked mocks with continua and experimental noise. Fig. 9 presents the $\text{Ly}\alpha \times \text{Ly}\alpha$ correlation for the 30 realizations of cooked mocks. The analysis was performed in 4 bins in redshift and the results are presented in 4 bins in μ . Comparing to Fig. 5 we note that the correlation function is considerably distorted by the fact that we have to fit the quasar continuum. This distortion is taken into account by the distortion matrix and the correlation function are rather well fit over the range $20 < r < 180h^{-1}$ Mpc by picca model with χ^2 of 1498, 1622, 1598, and 1629 in the four bins in redshift for 1570 degrees of freedom. The bias parameters, shown as the blue points in Fig. 6 are in good agreements with expectations and with the values derived for the raw mocks.

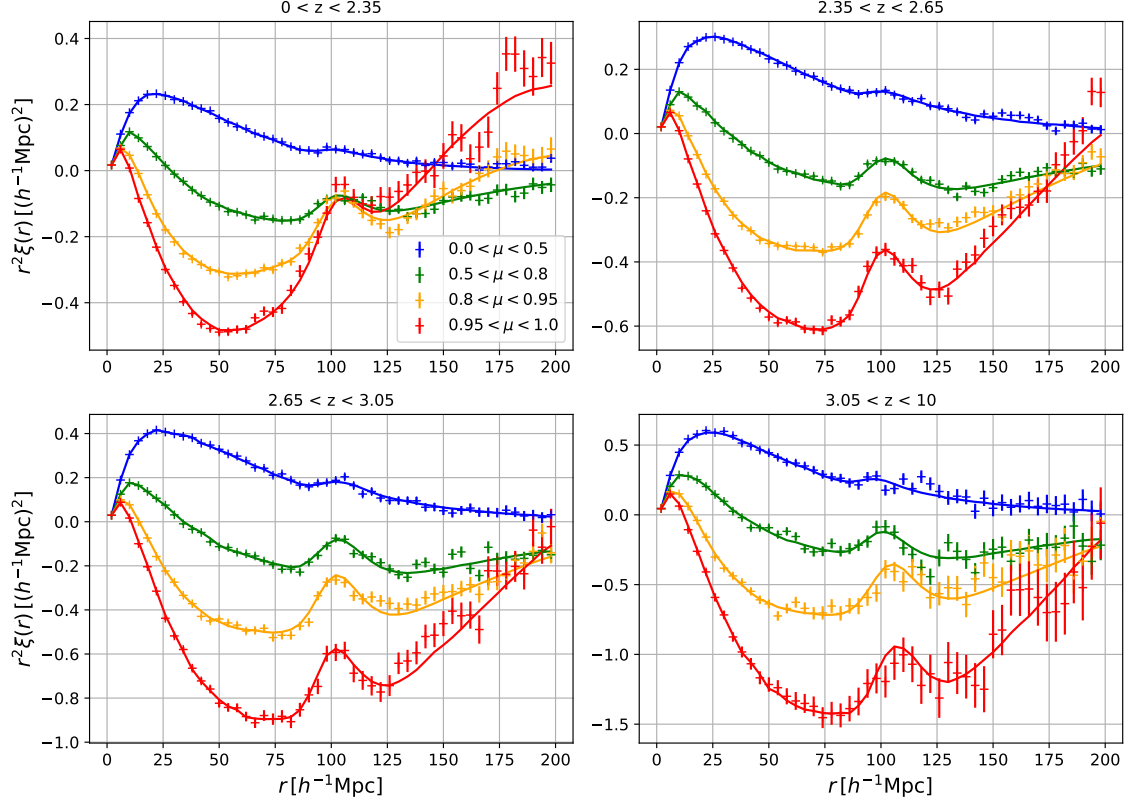


Figure 9. The same as Fig. 5 except now for the cooked mocks. Each graph gives the average of the correlation functions calculated in each redshift bins. The correlation functions are presented in four bins in μ . The continuous lines are the fits with picca model.

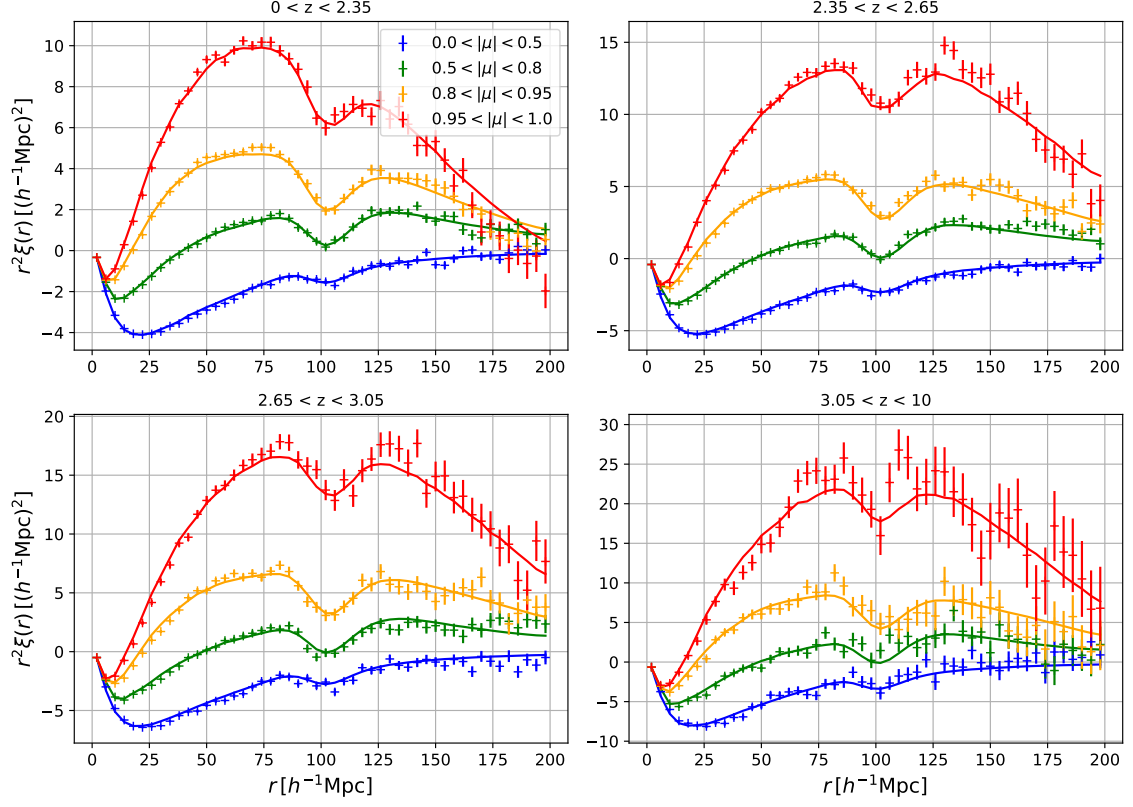


Figure 10. The Ly α x QSO cross-correlation for 30 realizations of cooked mocks. Each graph gives the average of the correlation functions calculated in each redshift bins. The correlation functions are presented in four bins in μ . The continuous lines are the fits with picca model.

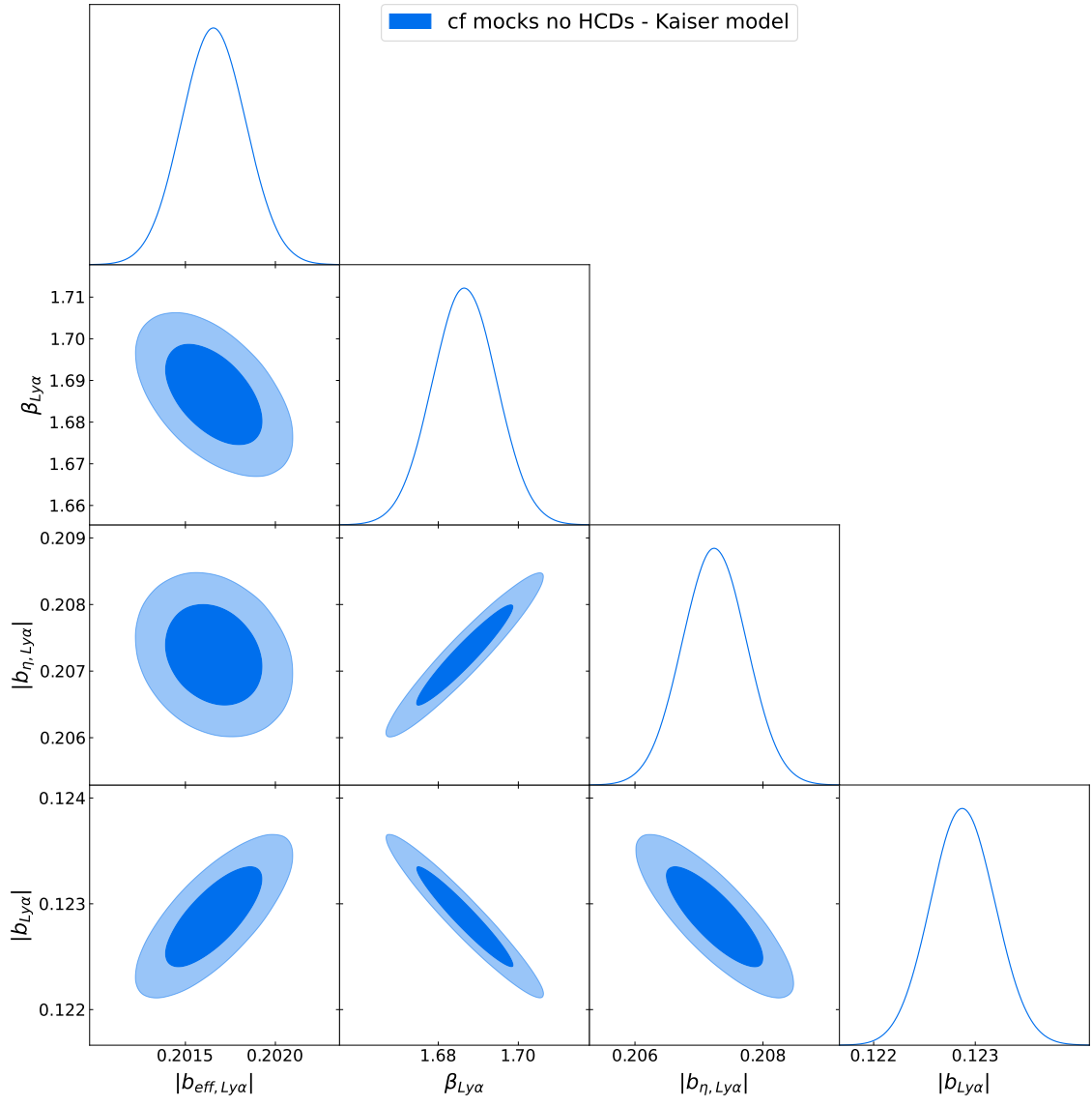


Figure 11. Correlations between the best-fit bias parameters of the auto-correlations

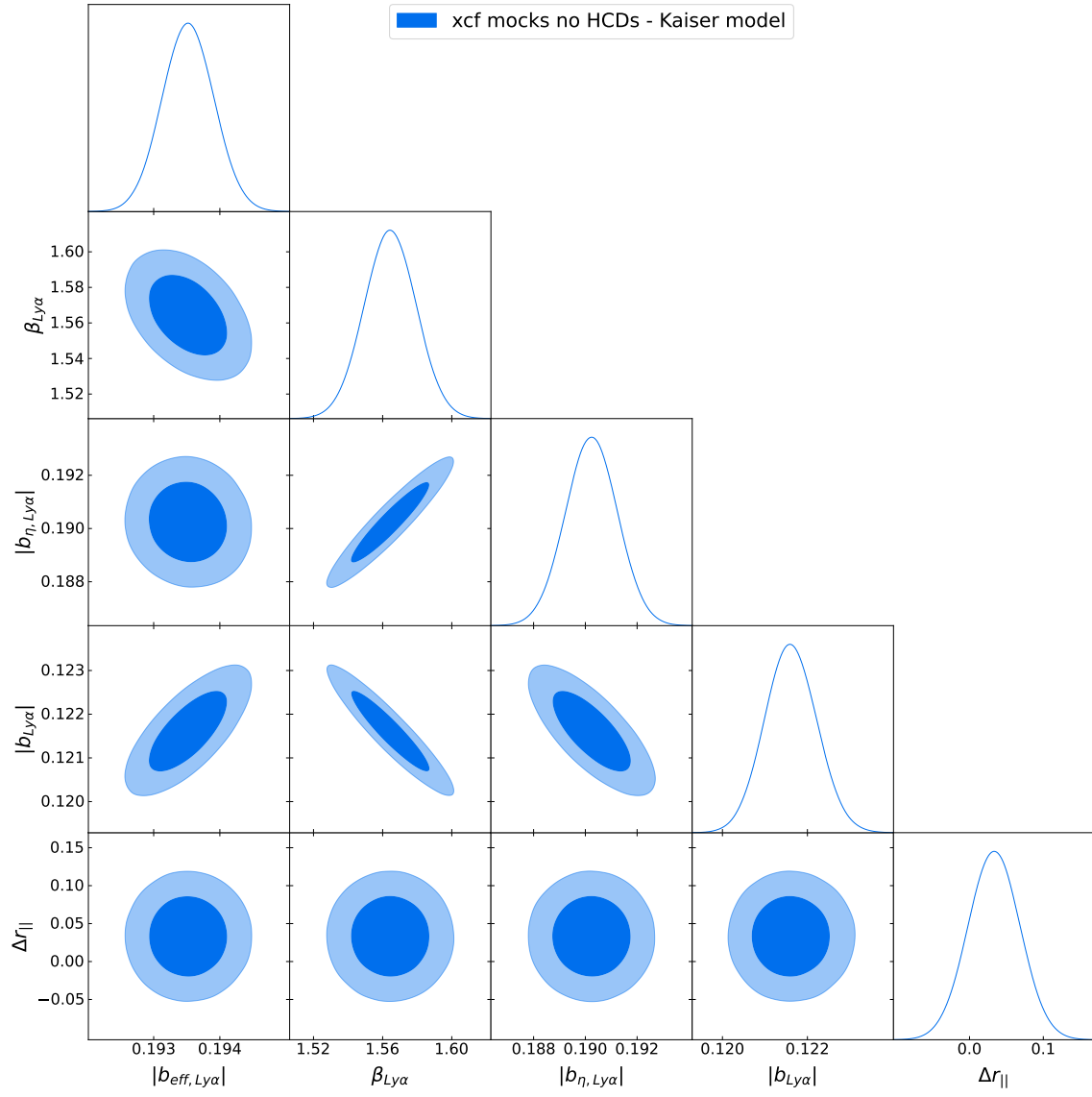


Figure 12. Same as Fig. 11 but for the cross-correlations

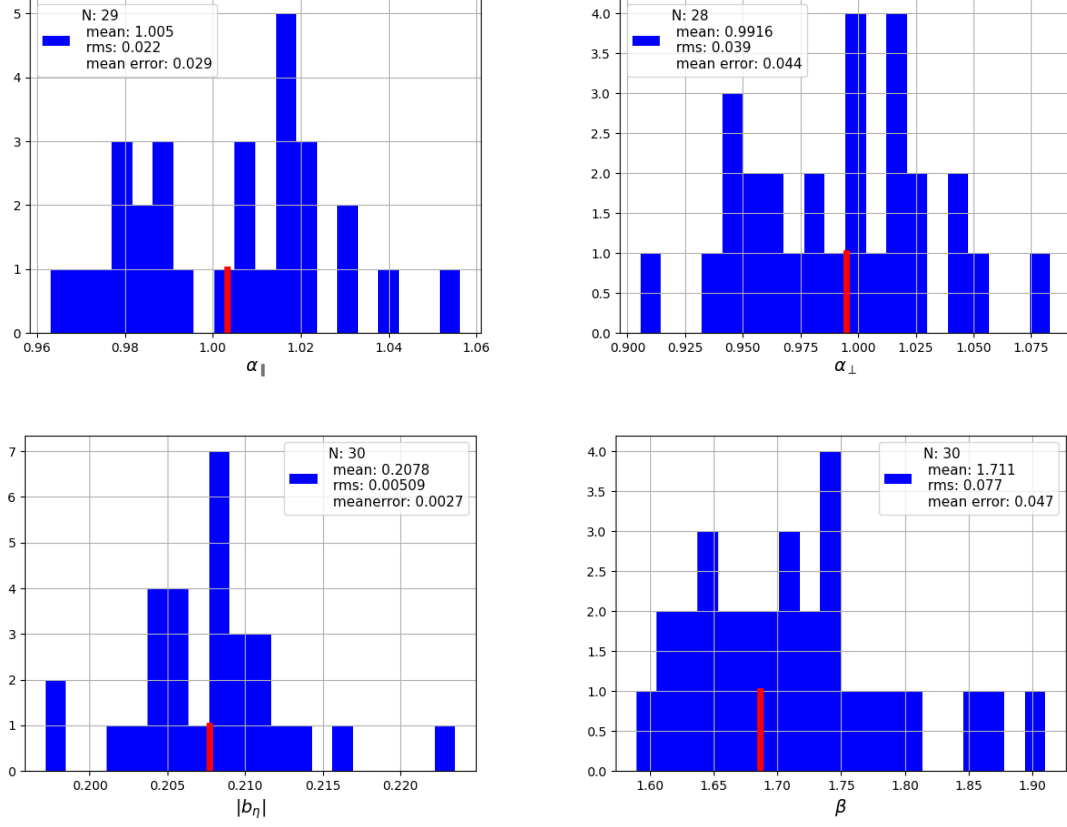


Figure 13. The distributions of fit parameters for the auto-correlation for the 30 Ly α -only mocks. The red entry shows the fit value for the stack of 30 mocks. The upper right corner lists the number of mocks included, the mean and standard deviation of the distribution, and the mean error reported by the fitter. One outlier is not included in the $\alpha_{||}$ distribution ($\alpha_{||} = 1.50 \pm 0.12$) and two outliers in the α_{\perp} distribution (1.39 ± 0.17 and 0.895 ± 0.040).

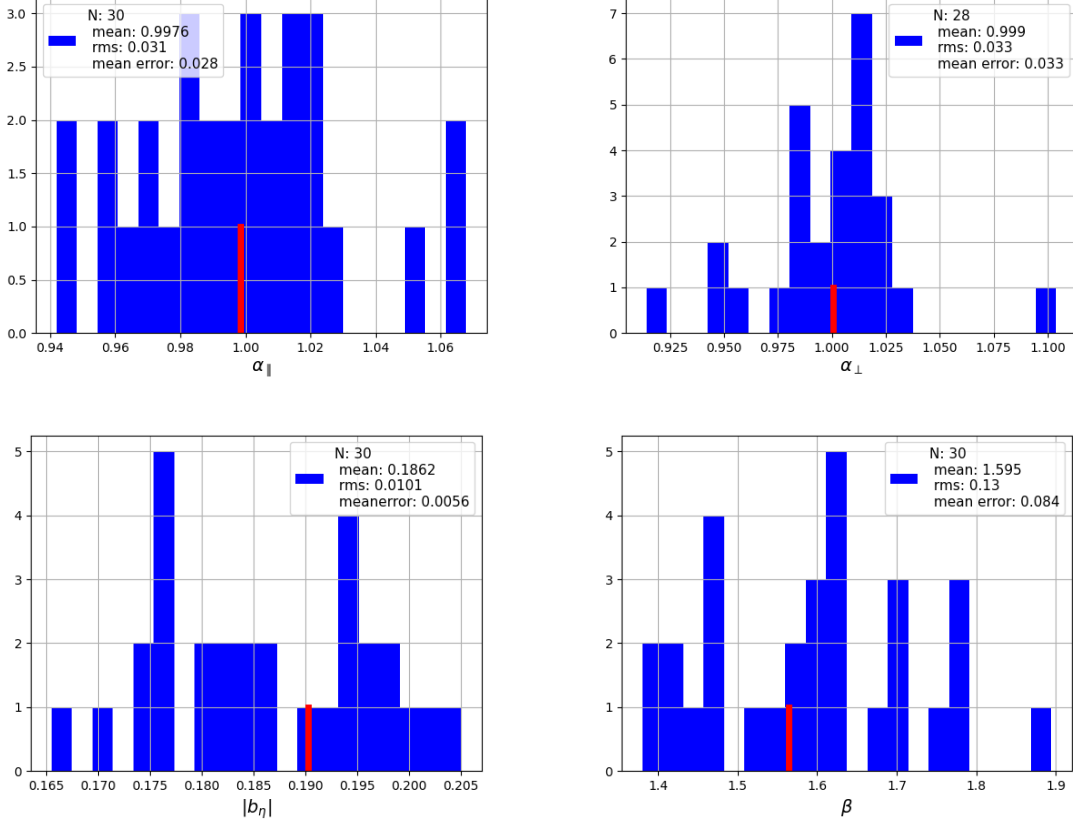


Figure 14. Same as Fig. 13 except now for the cross-correlation. Two outliers are not included in the α_{\perp} distribution ($\alpha_{\perp} = 1.31 \pm 0.08$ and $\alpha_{\perp} = 1.32 \pm 0.07$)

Fig. 10 presents the quasar-Ly α cross-correlation for a set of 30 realizations of cooked mocks with continuum and noise. As with the auto-correlation, the analysis was performed in 4 bins in redshift and the results are presented in 4 bins in μ . These cross correlations are rather well fit over the range $20 < r < 180h^{-1}$ Mpc by the picca model with χ^2 of 3233, 3410, 3228, 3410 in the four bins in redshift for 3143 degrees of freedom. The bias parameters shown in Fig. 12 are in agreement with those found for the raw mocks but, again, the values of β are about 10% lower than expected.

The correlations between the best-fit values of the bias parameters are shown in Figs. 11 and 12. We see that for both the auto- and cross-correlations, the most uncorrelated parameters are b_{eff} and b_{η} .

In the standard BAO analysis [13], the primary purpose of the mocks is to verify that the analysis procedure returns unbiased values of the model parameters and realistic uncertainties. Figure 13 shows the distribution of the best-fit parameters for the auto-correlation along with the mean of the reported errors. We see that for the BAO parameters, the mean returned values are both near the expected values of unity, and the standard deviation of the distributions are consistent with the mean of the reported uncertainties. However, for α_{\perp} , this is obtained only after eliminating two outlier realizations with large errors (1.39 ± 0.17 and 0.895 ± 0.040). For α_{\parallel} , one realization was eliminated with $\alpha_{\parallel} = 1.50 \pm 0.12$. We conclude that for data samples of the eBOSS size the measurement of the BAO-peak position is sufficiently fragile to give significant deviations from expectations in of order 10% of realizations. As first noted in [11], this also

results in slightly non-Gaussian errors for α_{\parallel} and α_{\perp} .

For the two bias parameters, the reported uncertainties are nearly a factor two smaller than the standard deviation of the distributions, implying that the procedure significantly underestimates the uncertainties in these parameters. We note, however, that the errors on real data are likely to be dominated by model uncertainties due to effects not included in these mocks, e.g. HCDs [Tan et al, in preparation].

Similar conclusions can be drawn for the cross-correlation as illustrated in Fig. 14.

4.4 QSO auto-correlations

The quasar-quasar auto correlations were measured using the standard techniques of comparing the observed distribution of object pairs with random catalogs (Landy-Szalay statistic) as described, for instance, in [38]. The auto-correlation was then fit with a Λ CDM-based model with bias parameters b_{QSO} and $\beta_{QSO} = fb_{\eta QSO}/b_{QSO}$ where $f \approx 1$ is the growth rate at $z \approx 2.3$ and $b_{\eta QSO} \approx 1$ is the velocity bias. In the fits, the Λ CDM value of the growth rate was not imposed so the fits yielded independent values of b_{QSO} and β_{QSO} .

Computing the auto-correlation of the quasars is rather CPU consuming and the mocks presented in this paper are not made to test the measurement of quasar auto-correlation. Therefore the auto-correlation was computed for only 10 realizations. The result is presented in Fig. 15. The right panel shows the correlation averaged over all bins in μ , which is very close to the prediction (Sect. 2.2), there is only a difference smaller than 2% at $r < 20h^{-1}$ Mpc. The agreement is not as good in wedges in μ , where the disagreement at small r reaches up to 12% (left panel).

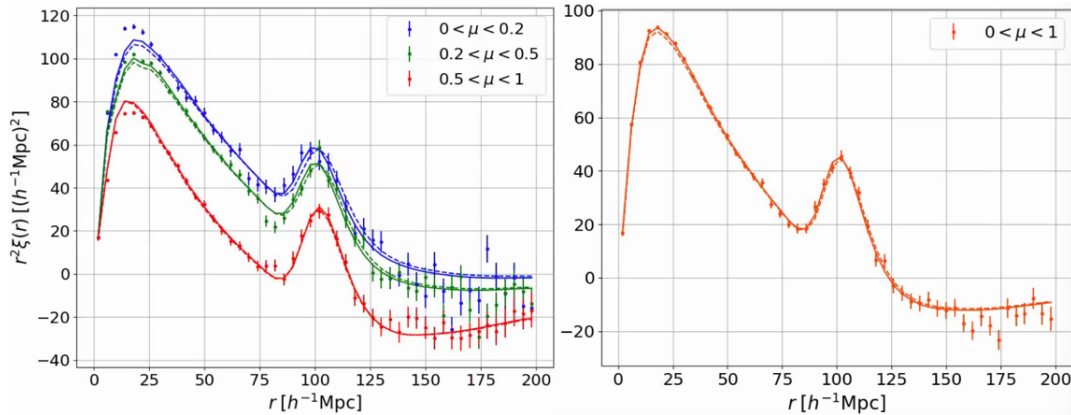


Figure 15. The QSO auto-correlation of 10 mock realizations averaged over the four redshift bins. The left panel presents the correlation in three bins in μ and the right one the average over the whole range in μ . The continuous lines give the fit by picca model and the dashed lines the prediction (Sect. 2.2)

The quasar auto-correlation in each redshift bin was fit over the range $20 < r < 180h^{-1}$ Mpc, resulting in the bias and RSD parameters displayed in Fig. 16. The χ^2 relative to the input parameterization are 10.8 for the bias and 4.2 for the RSD parameters for four degrees of freedom. The rather large χ^2 for the bias comes from the first two redshift points, which are low by 2.6 and 1.8 σ , but this corresponds to only 1.7 and 0.9% of the bias, respectively.

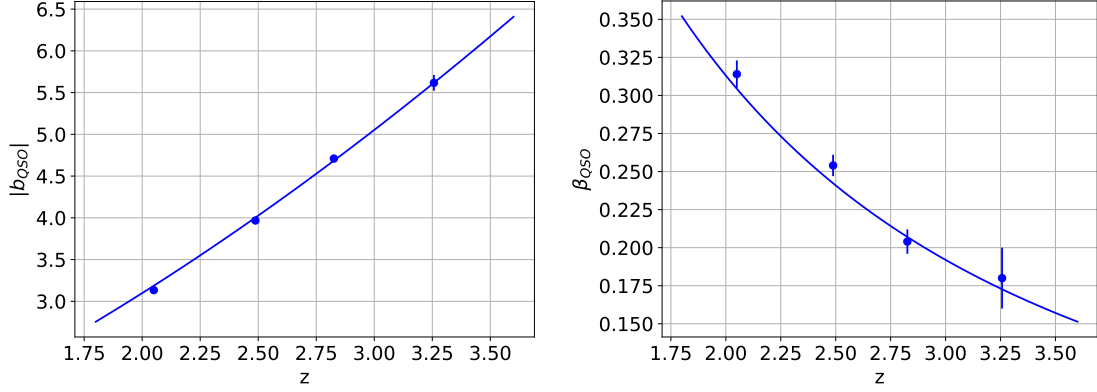


Figure 16. QSO bias (left panel) and QSO RSD parameter (right panel) versus redshift. The continuous lines are the input parameterizations used to build the mocks.

5 Conclusions

We have developed a set of codes to produce Ly α forest mock data sets using FFT to generate a Gaussian random field with the power spectrum of matter density fluctuations at $z = 0$. We use the corresponding linear velocity gradient η to implement RSD, which implies producing 6 coordinate fields since η is a tensor, in addition to the 3 velocity fields which are needed for the quasar velocity. This implementation of RSD is done through a modified FGPA, $F = \exp[-a \exp b(\delta + c\eta_{\parallel})]$. A nice feature of such an implementation is that it allows for a prediction (section 2.5) of the correlation function that is consistent with the measured mock correlation function within eBOSS error bars for $r > 20h^{-1}$ Mpc. The quasar locations are drawn using interpolation between lognormal density fields at three different redshifts. The production is split into a CPU-expensive pre-production step that draws quasar locations and computes δ and η_{\parallel} spectra along quasar line-of-sights, and a much faster post-production step, where the FGPA is applied. The code is not parallelized over several CPU nodes, which limits the available memory and then the volume of the data set. With $2.19h^{-1}$ Mpc voxels, five chunks are needed to cover the NGC and two for the SGC.

The resulting mock data sets generally fit well the desired characteristics with a few issues, typically at $r < 20h^{-1}$ Mpc. The mean transmitted flux fraction, $\overline{F}(z)$ is close to the input parameterization (Fig. 3). The quasar autocorrelation monopole is well-described by linear theory while the quadrupole is somewhat too large for $r < 20h^{-1}$ Mpc (Fig 15). The evolution of the quasar bias and the RSD parameter follow the input parameterizations (Fig. 16). The Ly α autocorrelation in four bins in z , times four wedges in $\mu = r_{\parallel}/r$, is consistent with the prediction (section 2.5) down to $r = 20h^{-1}$ Mpc and is well fit by the analysis pipeline model down to $r \approx 4h^{-1}$ Mpc (Fig. 5).

We aimed at reproducing the bias, $b_{eff}(z)$, and RSD parameter, $\beta(z)$, measured in eBOSS DR16 data and our raw and cooked mocks do reproduce these dependencies at the 5% level for the auto-correlation (Fig. 6). For the cross-correlation, we also obtained good agreement for $b_{eff}(z)$ but found a 10% disagreement for $\beta(x)$ (Fig. 8)

Acknowledgements

It is a pleasure to thank Nicolas Busca, Helion du Mas des Bourboux and Anze Slosar for important contributions during the early stages of this work. We thank Julian Bautista and the

anonymous referee for comments on the manuscript.

This material is based upon work supported by the U.S. Department of Energy (DOE), Office of Science, Office of High-Energy Physics, under Contract No. DE-AC02-05CH11231, and by the National Energy Research Scientific Computing Center, a DOE Office of Science User Facility under the same contract. Additional support for DESI was provided by the U.S. National Science Foundation (NSF), Division of Astronomical Sciences under Contract No. AST-0950945 to the NSF’s National Optical-Infrared Astronomy Research Laboratory; the Science and Technology Facilities Council of the United Kingdom; the Gordon and Betty Moore Foundation; the Heising-Simons Foundation; the French Alternative Energies and Atomic Energy Commission (CEA); the National Council of Science and Technology of Mexico (CONACYT); the Ministry of Science and Innovation of Spain (MICINN), and by the DESI Member Institutions: <https://www.desi.lbl.gov/collaborating-institutions>. Any opinions, findings, and conclusions or recommendations expressed in this material are those of the author(s) and do not necessarily reflect the views of the U. S. National Science Foundation, the U. S. Department of Energy, or any of the listed funding agencies.

The authors are honored to be permitted to conduct scientific research on Iolkam Du’ag (Kitt Peak), a mountain with particular significance to the Tohono O’odham Nation.

Data Points

The data points corresponding to each figure in this paper can be accessed in the Zenodo repository at <https://doi.org/10.5281/zenodo.8434293>.

A The z -dependence of quasar correlation function

As discussed in section 2.2, drawing quasars proportional to the field $\exp(\delta_q)$ results in a correlation function $\xi_0(r) = b_q^2(z_0)G^2(z_0)\xi_m(r, z=0)$. We aim at producing quasars with a model correlation function that depends on redshift, $\xi_{mod}(r, z) = b_q^2(z)G^2(z)\xi_m(r, z=0)$. This dependence can be introduced by drawing quasars with a probability proportional to the field $p = \exp[a(z)\delta_q]$ with $a(z) = \sqrt{\xi_{mod}(r, z)/\xi_0} = b_q(z)(1+z_0)/[b_q(z_0)(1+z)]$, which results in a correlation function $\xi_p(r, z) = \exp[a^2(z)\xi(\delta_q)] - 1$. Since $\xi_0 = \xi[\exp \delta_q] = \exp[\xi(\delta_q)] - 1$ we have

$$\xi_p(r, z) = \exp[a^2(z) \ln(1 + \xi_0)] - 1 = (1 + \xi_0)^{a^2} - 1 \approx a^2 \xi_0 \left(1 + \frac{a^2 - 1}{2} \xi_0\right). \quad (\text{A.1})$$

If either $\xi_0 \ll 1$ or $|a - 1| \ll 1$, this is producing quasars with a correlation function $a^2(z)\xi_0 = \xi_{mod}(r, z)$, which is what we want. The deviations are, however, significant at low values of r when z is significantly different from z_0 . For instance for $z_0 = 2.33$ and $z = 3.6$ there is a 18% deviation at $r = 10h^{-1}$ Mpc.

A better result is obtained by producing two quasar-density boxes δ_{q1} at z_1 and δ_{q2} at $z_2 > z_1$. We define field $p_1 = \exp[a_1(z)\delta_{q1}]$ with $a_1 = b_q(z)(1+z_1)/[b_q(z_1)(1+z)]$, which has correlation function ξ_1 , and define field p_2 in a similar way. At a given z between z_1 and z_2 , we then draw quasars with a probability proportional to the field p_{12} that is the linear interpolation of p_1 and p_2 as a function of z , resulting in a correlation function ξ_{12} that is the linear interpolation of ξ_1 and ξ_2 . This ξ_{12} is slightly lower than $\xi_{mod}(z)$ (orange curve in Fig. 17 left). On the other hand, if we have a third field p_3 at $z_3 > z_2$, combining p_2 and p_3 to extrapolate outside the range $[z_2, z_3]$ down to z , results in ξ_{23} that is slightly larger than $\xi_{mod}(z)$ (blue curve in Fig. 17 left). The shape of these under and over-estimations as a function of r happen to be very close. So finally we produce three quasar-density boxes at $z_1 = 1.9$, $z_2 = 2.75$ and $z_3 = 3.6$. To produce

the probability field at e.g. $z = 2.3$, we combine the field p_{12} from the interpolation between z_1 and z_2 and the field p_{23} from the extrapolation from z_2 and z_3 , with coefficients that exactly compensate the under and the over-estimates at $r = 5h^{-1}$ Mpc. As a result, we get the model correlation function at better than 5×10^{-4} down to $r = 5h^{-1}$ Mpc as can be seen in Fig. 17 right.

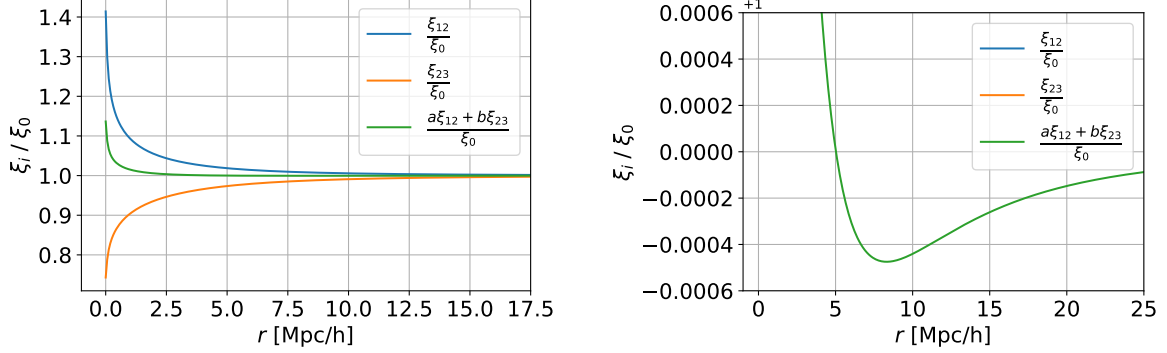


Figure 17. The ratio ξ_{12}/ξ_{mod} (blue) and ξ_{23}/ξ_{mod} (orange) at $z = 2.38$. For this redshift, ξ_{12} is the linear interpolation of ξ_1 and ξ_2 and ξ_{23} the linear extrapolation of ξ_2 and ξ_3 . The green curve is obtained as a linear combination of ξ_{12} and ξ_{23} , see text for details. The redshift $z = 2.38$ is the redshift for which the green curve deviates the most from ξ_{mod} . The right graph is a zoom of the left one.

B Small scale fluctuations

The 1d power spectrum is an integral of the 3d power spectrum over k_\perp [54],

$$P^{1d}(k_\parallel) = \frac{1}{2\pi} \int_0^\infty P(k_\parallel, k_\perp) k_\perp dk_\perp . \quad (\text{B.1})$$

In our mocks P actually includes both the squared voxel window $W^2(k) = \text{sinc}^2(ak_x/2) \times \text{sinc}^2(ak_y/2) \text{sinc}^2(ak_z/2)$ and the squared Gaussian smoothing window $W^2(k) = \exp(-a^2 k^2)$. These window functions cancel high- k contributions to the integral and, since the integral goes to infinity and P is multiplied by a factor k_\perp , they strongly reduce $P^{1d}(k_\parallel)$, as illustrated in Fig. 18.

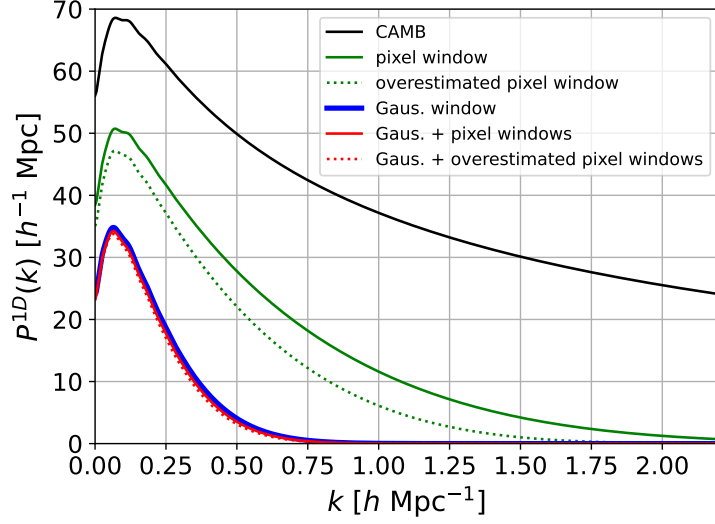


Figure 18. P^{1d} power spectrum from CAMB (black), same including the voxel size ($a = 2.19h^{-1}$ Mpc) window (green), the Gaussian window (blue) and both of them (red). In the cases where the voxel size window is included (green and red curves), the continuous curves correspond to the approximation $W = \text{sinc}^3(ka/2\sqrt{3})$ (see section 2.5), while the dotted curve corresponds to the window of a sphere of radius $\sqrt{3}a$, which is underestimating the window function.

It may seem surprising that, as pointed in section 2, the effect of the window function is hardly visible in a plot of $r^2\xi^{3d}(r)$. The point is that there is a strong effect also on $\xi^{3d}(r)$, in particular $\xi^{3d}(r=0) = \xi^{1d}(r=0)$ is the strongly reduced pixel variance. But since ξ^{3d} is the Fourier transform of P^{3d} , when r is large the factor $\exp(-ikr)$ kills the contribution of large k modes for which $W(k)$ is significantly different from unity. The effect of $W(k)$ is then limited to small r values, which are not visible in a plot of $r^2\xi(r)$ and which are not of interest for BAO analyses. In contrast in Eq B.1 there is no factor $\exp(ikr)$ and on the contrary there is a factor k_{\perp} , which is increasing the contribution of large k modes.

References

- [1] Dawson, K. S., D. J. Schlegel, C. P. Ahn, et al. The Baryon Oscillation Spectroscopic Survey of SDSS-III. *Astronom. J.*, 145:10, 2013. [arXiv:1208.0022](#).
- [2] Dawson, K. S., J.-P. Kneib, W. J. Percival, et al. The SDSS-IV Extended Baryon Oscillation Spectroscopic Survey: Overview and Early Data. *Astronom. J.*, 151:44, 2016. [arXiv:1508.04473](#).
- [3] Slosar, A., A. Font-Ribera, M. M. Pieri, et al. The Lyman- α forest in three dimensions: measurements of large scale flux correlations from BOSS 1st-year data. *JCAP*, 2011:001, 2011. [arXiv:astro-ph.CO/1104.5244](#).
- [4] Busca, N. G., T. Delubac, J. Rich, et al. Baryon acoustic oscillations in the Ly α forest of BOSS quasars. *Astron. and Astrophys.*, 552:A96, 2013. [arXiv:astro-ph.CO/1211.2616](#).
- [5] Slosar, A., V. Iršič, D. Kirkby, et al. Measurement of baryon acoustic oscillations in the Lyman- α forest fluctuations in BOSS data release 9. *JCAP*, 2013:026, 2013. [arXiv:astro-ph.CO/1301.3459](#).
- [6] Delubac, T., J. E. Bautista, N. G. Busca, et al. Baryon acoustic oscillations in the Ly α forest of BOSS DR11 quasars. *Astron. and Astrophys.*, 574:A59, 2015. [arXiv:astro-ph.CO/1404.1801](#).

- [7] Bautista, J. E., N. G. Busca, J. Guy, et al. Measurement of baryon acoustic oscillation correlations at $z = 2.3$ with SDSS DR12 Ly α -Forests. *Astron. and Astrophys.*, 603:A12, 2017. [arXiv:astro-ph.CO/1702.00176](#).
- [8] de Sainte Agathe, V., C. Balland, H. du Mas des Bourboux, et al. Baryon acoustic oscillations at $z = 2.34$ from the correlations of Ly α absorption in eBOSS DR14. *Astron. and Astrophys.*, 629:A85, 2019. [arXiv:astro-ph.CO/1904.03400](#).
- [9] Font-Ribera, A., E. Arnau, J. Miralda-Escudé, et al. The large-scale quasar-Lyman α forest cross-correlation from BOSS. *JCAP*, 5:018, 2013. [arXiv:1303.1937](#).
- [10] Font-Ribera, A., D. Kirkby, N. Busca, et al. Quasar-Lyman α forest cross-correlation from BOSS DR11: Baryon Acoustic Oscillations. *JCAP*, 2014:027, 2014. [arXiv:astro-ph.CO/1311.1767](#).
- [11] du Mas des Bourboux, H., J.-M. Le Goff, M. Blomqvist, et al. Baryon acoustic oscillations from the complete SDSS-III Ly α -quasar cross-correlation function at $z = 2.4$. *Astron. and Astrophys.*, 608:A130, 2017. [arXiv:1708.02225](#).
- [12] Blomqvist, M., H. du Mas des Bourboux, N. G. Busca, et al. Baryon acoustic oscillations from the cross-correlation of Ly α absorption and quasars in eBOSS DR14. *Astron. and Astrophys.*, 629:A86, 2019. [arXiv:astro-ph.CO/1904.03430](#).
- [13] du Mas des Bourboux, H., J. Rich, A. Font-Ribera, et al. The Completed SDSS-IV Extended Baryon Oscillation Spectroscopic Survey: Baryon Acoustic Oscillations with Ly α Forests. *Astrophys. J.*, 901:153, 2020. [arXiv:astro-ph.CO/2007.08995](#).
- [14] Alam, S., M. Aubert, S. Avila, et al. Completed SDSS-IV extended Baryon Oscillation Spectroscopic Survey: Cosmological implications from two decades of spectroscopic surveys at the Apache Point Observatory. *Phys. Rev. D*, 103:083533, 2021. [arXiv:astro-ph.CO/2007.08991](#).
- [15] Font-Ribera, A., J. Miralda-Escudé, E. Arnau, et al. The large-scale cross-correlation of Damped Lyman alpha systems with the Lyman alpha forest: first measurements from BOSS. *JCAP*, 2012:059, 2012. [arXiv:astro-ph.CO/1209.4596](#).
- [16] Pérez-Ràfols, I., A. Font-Ribera, J. Miralda-Escudé, et al. The SDSS-DR12 large-scale cross-correlation of damped Lyman alpha systems with the Lyman alpha forest. *Mon. Not. Roy. Astron. Soc.*, 473:3019–3038, 2018. [arXiv:astro-ph.CO/1709.00889](#).
- [17] Pérez-Ràfols, I., M. M. Pieri, M. Blomqvist, et al. The cross-correlation of galaxies in absorption with the Lyman α forest. *arXiv e-prints*, page arXiv:2210.02973, 2022. [arXiv:astro-ph.CO/2210.02973](#).
- [18] Croft, R. A. C., D. H. Weinberg, N. Katz, et al. Recovery of the Power Spectrum of Mass Fluctuations from Observations of the Ly α Forest. *Astrophys. J.*, 495:44–62, 1998. [arXiv:astro-ph/9708018](#).
- [19] McDonald, P., J. Miralda-Escudé, M. Rauch, et al. The Observed Probability Distribution Function, Power Spectrum, and Correlation Function of the Transmitted Flux in the Ly α Forest. *Astrophys. J.*, 543:1–23, 2000. [arXiv:astro-ph/astro-ph/9911196](#).
- [20] Chabanier, S. et al. The one-dimensional power spectrum from the SDSS DR14 Ly α forests. *JCAP*, 07:017, 2019. [arXiv:astro-ph.CO/1812.03554](#).
- [21] Ravoux, C., M. L. A. Karim, E. Armengaud, et al. The Dark Energy Spectroscopic Instrument: One-dimensional power spectrum from first Lyman- α forest samples with Fast Fourier Transform. *arXiv e-prints*, page arXiv:2306.06311, 2023. [arXiv:astro-ph.CO/2306.06311](#).
- [22] Karaçaylı, N. G., P. Martini, J. Guy, et al. Optimal 1D Ly α Forest Power Spectrum Estimation – III. DESI early data. *arXiv e-prints*, page arXiv:2306.06316, 2023. [arXiv:astro-ph.CO/2306.06316](#).
- [23] Abareschi, B. et al. Overview of the Instrumentation for the Dark Energy Spectroscopic Instrument. *Astron. J.*, 164:207, 2022. [arXiv:astro-ph.IM/2205.10939](#).

- [24] DESI Collaboration, A. G. Adame, J. Aguilar, et al. Validation of the Scientific Program for the Dark Energy Spectroscopic Instrument. *arXiv e-prints*, page arXiv:2306.06307, 2023. [arXiv:astro-ph.CO/2306.06307](#).
- [25] Font-Ribera, A., P. McDonald, and J. Miralda-Escudé. Generating mock data sets for large-scale Lyman- α forest correlation measurements. *JCAP*, 1:1, 2012. [arXiv:1108.5606](#).
- [26] Bautista, J. E., S. Bailey, A. Font-Ribera, et al. Mock Quasar-Lyman- α forest data-sets for the SDSS-III Baryon Oscillation Spectroscopic Survey. *JCAP*, 2015:060–060, 2015. [arXiv:astro-ph.CO/1412.0658](#).
- [27] Le Goff, J. M., C. Magneville, E. Rollinde, et al. Simulations of BAO reconstruction with a quasar Ly- α survey. *Astron. and Astrophys.*, 534:A135, 2011. [arXiv:astro-ph.CO/1107.4233](#).
- [28] de Sainte Agathe, V., C. Balland, H. du Mas des Bourboux, et al. Baryon acoustic oscillations at $z = 2.34$ from the correlations of Ly α absorption in eBOSS DR14. *Astron. and Astrophys.*, 629:A85, 2019. [arXiv:astro-ph.CO/1904.03400](#).
- [29] Blomqvist, M., H. du Mas des Bourboux, N. G. Busca, et al. Baryon acoustic oscillations from the cross-correlation of Ly α absorption and quasars in eBOSS DR14. *Astron. and Astrophys.*, 629:A86, 2019. [arXiv:astro-ph.CO/1904.03430](#).
- [30] Farr, J., A. Font-Ribera, H. du Mas des Bourboux, et al. LyaCoLoRe: Synthetic Datasets for Current and Future Lyman- α Forest BAO Surveys. *arXiv e-prints*, page arXiv:1912.02763, 2019. [arXiv:astro-ph.CO/1912.02763](#).
- [31] Chabanier, S., T. Etourneau, J.-M. Le Goff, et al. The Completed Sloan Digital Sky Survey IV Extended Baryon Oscillation Spectroscopic Survey: The Damped Ly α Systems Catalog. *Astrophys. J. Suppl.*, 258:18, 2022. [arXiv:astro-ph.CO/2107.09612](#).
- [32] Ravoux, C., E. Armengaud, J. Bautista, et al. First measurement of the correlation between cosmic voids and the Lyman- α forest. *arXiv e-prints*, page arXiv:2203.11045, 2022. [arXiv:astro-ph.CO/2203.11045](#).
- [33] Herrera-Alcantar, H. K., A. Muñoz-Gutiérrez, T. Tan, et al. Synthetic spectra for Lyman- α forest analysis in the Dark Energy Spectroscopic Instrument. *arXiv e-prints*, page arXiv:2401.00303, 2023. [arXiv:astro-ph.CO/2401.00303](#).
- [34] Planck Collaboration, N. Aghanim, Y. Akrami, et al. Planck 2018 results. VI. Cosmological parameters. *Astron. and Astrophys.*, 641:A6, 2020. [arXiv:astro-ph.CO/1807.06209](#).
- [35] Cooley, J. W. and J. W. Tukey. An algorithm for the machine calculation of complex Fourier series. *Mathematics of Computation*, 19:297–301, 1965. URL: <http://cr.yp.to/bib/entries.html#1965/cooley>.
- [36] Lewis, A., A. Challinor, and A. Lasenby. Efficient Computation of Cosmic Microwave Background Anisotropies in Closed Friedmann-Robertson-Walker Models. *Astrophys. J.*, 538:473–476, 2000. [astro-ph/9911177](#).
- [37] Padmanabhan, T. *Structure Formation in the Universe*. Cambridge University Press, 1993.
- [38] Laurent, P., S. Eftekharzadeh, J.-M. Le Goff, et al. Clustering of quasars in SDSS-IV eBOSS: study of potential systematics and bias determination. *JCAP*, 2017:017, 2017. [arXiv:astro-ph.CO/1705.04718](#).
- [39] Coles, P. and B. Jones. A lognormal model for the cosmological mass distribution. *Mon. Not. Roy. Astron. Soc.*, 248:1–13, 1991.
- [40] Weinberg, D. and et al. Cosmological tests with the Ly- α forest (invited review). In Banday, A. J., R. K. Sheth, and L. N. da Costa, editors, *Evolution of Large Scale Structure : From Recombination to Garching*, page 346, 1999, [arXiv:astro-ph/astro-ph/9810142](#).
- [41] Hui, L. and N. Y. Gnedin. Equation of state of the photoionized intergalactic medium. *Mon. Not. Roy. Astron. Soc.*, 292:27–+, 1997.

- [42] Bi, H. and A. F. Davidsen. Evolution of Structure in the Intergalactic Medium and the Nature of the Ly α Forest. *Astrophys. J.*, 479:523–+, 1997. [arXiv:astro-ph/9611062](#).
- [43] Seljak, U. Bias, redshift space distortions and primordial nongaussianity of nonlinear transformations: application to Ly- α forest. *JCAP*, 2012:004, 2012. [arXiv:astro-ph.C0/1201.0594](#).
- [44] Cieplak, A. M. and A. Slosar. Towards physics responsible for large-scale Lyman- α forest bias parameters. *JCAP*, 2016:016, 2016. [arXiv:astro-ph.C0/1509.07875](#).
- [45] Hamilton, A. J. S. Measuring Omega and the real correlation function from the redshift correlation function. *Astrophys. J. Lett.*, 385:L5–L8, 1992.
- [46] Palanque-Delabrouille, N., C. Yèche, A. Borde, et al. The one-dimensional Ly α forest power spectrum from BOSS. *Astron. and Astrophys.*, 559:A85, 2013. [arXiv:astro-ph.C0/1306.5896](#).
- [47] Calura, F., E. Tescari, V. D’Odorico, et al. The Lyman α forest flux probability distribution at $z > 3$. *Mon. Not. Roy. Astron. Soc.*, 422:3019–3036, 2012. [arXiv:astro-ph.C0/1201.5121](#).
- [48] James, F. and M. Roos. Minuit - a system for function minimization and analysis of the parameter errors and correlations. *Computer Physics Communications*, 10:343–367, 1975.
- [49] Rogers, K. K., S. Bird, H. V. Peiris, et al. Correlations in the three-dimensional lyman-alpha forest contaminated by high column density absorbers. *Monthly Notices of the Royal Astronomical Society*, 476:3716–3728, 2018.
- [50] Font-Ribera, A. and J. Miralda-Escudé. The effect of high column density systems on the measurement of the Lyman- α forest correlation function. *JCAP*, 2012:028, 2012. [arXiv:astro-ph.C0/1205.2018](#).
- [51] Prochaska, J. X., N. Tejos, cwotta, et al. pyigm/pyigm: Initial release for publications, 2017. URL <https://doi.org/10.5281/zenodo.1045480>.
- [52] Prochaska, J. X., P. Madau, J. M. O’Meara, et al. Towards a unified description of the intergalactic medium at redshift $z \approx 2.5$. *Mon. Not. Roy. Astron. Soc.*, 438:476–486, 2014. [arXiv:astro-ph.C0/1310.0052](#).
- [53] McGreer, I., J. Moustakas, and J. Schindler. simqso: Simulated quasar spectra generator. Astrophysics Source Code Library, record ascl:2106.008, 2021, [ascl:2106.008](#).
- [54] Kaiser, N. and J. A. Peacock. Power-spectrum analysis of one-dimensional redshift surveys. *Astrophys. J.*, 379:482–506, 1991.